

# Plasma expansion into vacuum assuming a steplike electron energy distribution

Thomas Kiefer,<sup>1,\*</sup> Theodor Schlegel,<sup>2,3</sup> and Malte C. Kaluza<sup>1,3</sup>

<sup>1</sup>*Friedrich-Schiller-Universität Jena, Jena, Germany*

<sup>2</sup>*GSF Helmholtzzentrum für Schwerionenforschung GmbH, Darmstadt, Germany*

<sup>3</sup>*Helmholtz-Institut Jena, Jena, Germany*

(Received 28 November 2012; revised manuscript received 8 March 2013; published 22 April 2013)

The expansion of a semi-infinite plasma slab into vacuum is analyzed with a hydrodynamic model implying a steplike electron energy distribution function. Analytic expressions for the maximum ion energy and the related ion distribution function are derived and compared with one-dimensional numerical simulations. The choice of the specific non-Maxwellian initial electron energy distribution automatically ensures the conservation of the total energy of the system. The estimated ion energies may differ by an order of magnitude from the values obtained with an adiabatic expansion model supposing a Maxwellian electron distribution. Furthermore, good agreement with data from experiments using laser pulses of ultrashort durations  $\tau_L \lesssim 80$  fs is found, while this is not the case when a hot Maxwellian electron distribution is assumed.

DOI: [10.1103/PhysRevE.87.043110](https://doi.org/10.1103/PhysRevE.87.043110)

PACS number(s): 52.38.Kd, 52.50.Jm, 52.65.-y, 02.60.Cb

## I. INTRODUCTION

In physics and applied science there is a large interest in the production of highly energetic ions. In addition to the possibility of using conventional accelerators, laser-driven ion acceleration has gained increasing interest in recent years as a promising alternative. Although this idea was already discussed in the 1970s [1–4], the focus has been renewed with the first experiments using short-pulse high-power lasers [5–8]. The ion pulses produced in such experiments reveal several outstanding properties. They are characterized by (i) a short duration, which is initially of the order of the laser pulse length [5,7,9], and (ii) a small divergence angle [10], and they are (iii) highly laminar [11,12] and contain (iv) a large number of particles (e.g., up to  $10^{13}$  protons [13]). Due to these features laser-based particle accelerators may become auspicious sources for different applications such as in medical physics [14–16], for new diagnostic techniques [17–20], for astrophysical investigations of high-energy-density matter [21–24], for isotope production [25,26], as front ends for conventional accelerators [11,27], and for fast ignition in the context of inertial fusion energy research [28–34].

The dominant mechanism in most of the laser-driven ion acceleration experiments performed so far is the so-called target normal sheath acceleration (TNSA). In this scheme, a subpicosecond laser pulse with an intensity  $\gtrsim 10^{19}$  W/cm<sup>2</sup> ionizes atoms at the front side of a solid target and accelerates the electrons of this plasma layer to relativistic energies [35,36]. These hot electrons propagate through the target [37,38] and exit at its rear side, forming a plasma sheath. The associated charge separation causes a strong electrostatic field oriented normally to the target rear surface, which ionizes atoms in the vacuum-target surface layer and accelerates them up to energies in the range of several tens of MeV per nucleon [5].

In order to describe the ion acceleration process theoretically, numerous publications appeared during the past decade. Many of them are based on the pioneering articles by Gurevich, Allen, and Widner [1,39,40]. The theoretical analysis is often

reduced to a one-dimensional electrostatic description, in which the Poisson equation plays a central role. Moreover, the explicit dynamics of the electrons is usually neglected by assuming that the electrons arrange themselves in a stationary configuration with the electric potential. The basic relation, which describes the electron distribution in this case, is the stationary, one-dimensional, electrostatic Vlasov equation,

$$\frac{p}{m_e \gamma} \frac{\partial f_e}{\partial x} + e \frac{\partial \phi}{\partial x} \frac{\partial f_e}{\partial p} = 0, \quad (1a)$$

where  $f_e(x, p)$  expresses the phase-space density of the electrons,  $x$  is the spatial coordinate,  $p$  refers to the momentum in this direction, and  $\gamma = \sqrt{1 + (p/m_e c)^2}$  denotes the corresponding Lorentz factor. In addition, the notations  $m_e$  for the electron rest mass,  $e$  for the elementary charge, and  $\phi$  for the electric potential are used.

Note that the Vlasov equation (1a) has an infinite number of solutions given as

$$f_e(x, p) = f_{e,0}(\Omega(p, \phi)), \quad (1b)$$

with

$$\Omega(p, \phi) = c^{-1} \sqrt{(\gamma m_e c^2 - e \phi)^2 - (m_e c^2)^2}.$$

The distribution  $f_{e,0}$  is an arbitrary function of the momentum  $p$ , which has to fulfill the symmetry condition  $f_{e,0}(p) = f_{e,0}(-p)$ . It describes the phase-space density in the absence of an electric potential. Depending on the choice of  $f_{e,0}$  one may obtain different expressions for the electron density as a function of the potential

$$n_e(\phi) = \int_{\mathbb{R}} f_{e,0}(\Omega(p, \phi)) dp. \quad (1c)$$

So far, a density relation of the form  $n_e(\phi) = n_{e,0} \exp(e \phi / T_{e,0})$  has been used in many models (see, for example, Refs. [2,13,39–43]), with the electron temperature in energy units,<sup>1</sup>  $T_{e,0}$ , and the electron density  $n_{e,0}$ , both being the

\*kiefer.thomas@gmail.de

<sup>1</sup>In the following we label the thermal energy  $k_B T_{e,0}$  by  $T_{e,0}$  and refer to it shortly as a temperature.

respective equilibrium values in the absence of any potential ( $\phi = 0$ ). Using this approach, a Maxwellian distribution for  $f_{e,0}$  is assumed implicitly, as one can prove immediately after inserting the Maxwell-Jüttner distribution (see, e.g., Ref. [44]) in Eq. (1c). However, there is *a priori* no direct reason for this assumption, because the plasma can be treated to be collisionless in most experimental schemes relevant for laser-driven ion acceleration from solid targets [45]. In fact, there are experimental observations and theoretical arguments for a non-Maxwellian distribution [46–51]. In these studies, the plasma expansion was investigated assuming either a truncated Maxwellian distribution [46–49,51], a super-Gaussian distribution [52,53] or a Crain distribution [54]. Note that the form of the hot electron distribution to be used is still under debate [54,55].

In addition, there are contributions dealing with the laser-heated plasma expansion into vacuum taking both hot and cold electrons into account. Commonly, these studies are assuming a bi-Maxwellian electron distribution function (for example, see Refs. [3,13,42,56–60]). From these investigations it can be found that for typical values of the electron populations present in TNSA experiments,<sup>2</sup> the acceleration process at the ion front of the expanding plasma is strongly dominated by the hot electrons [59], since the cold electron population is almost completely left behind. Although there is a noticeable effect on the ion front caused by the cold electrons at the very beginning of the expansion, which leads to slightly higher ion energies in comparison with the case of a single hot electron distribution (see, e.g., Fig. 14 in Ref. [59]), the direct influence of the cold electrons on the qualitative properties of the ion front is almost negligible. In addition, to the weak direct influence, there is also an indirect effect on the ion front caused by the cold electrons. Due to these electrons, the temporal evolution of the hot electron phase-space density may differ from the case assuming a single hot electron distribution [57,60]. However, within the electron parameter range of our interest this effect becomes relevant only on a time-scale, which is larger than the typical effective ion acceleration time. From that we may reason that the qualitative behavior of the ion front acceleration is well described with one hot electron population only.

In this paper we analyze the free expansion of a plasma assuming a single steplike hot electron energy distribution,<sup>3</sup> illustrating the significant modification of the ion acceleration process when a non-Maxwellian initial electron distribution is assumed. Note that the expansion of a plasma with such an electron phase-space density intrinsically conserves the total energy of the system [61]. Therefore, it might be an adequate ansatz for the description of the adiabatic plasma expansion. As it has been shown in Ref. [61], a steplike electron energy distribution implies the spatial electron density to have the form

$$n_e(\phi) = n_{e,0} \left( 1 + \frac{\kappa - 1}{\kappa} \frac{e\phi}{T_{e,0}} \right)^{1/(\kappa-1)}. \quad (2a)$$

<sup>2</sup>Commonly, the characteristic densities  $n_h, n_c$  and temperatures  $T_h, T_c$  of the hot and cold electron populations, respectively, fulfill the conditions  $n_h \ll n_c, T_h \gg T_c$  and  $n_h T_h \gtrsim n_c T_c$ .

<sup>3</sup>In the literature, the name “waterbag” distribution is also used.

Here,  $\kappa$  denotes the adiabatic index, which is determined by the degrees of freedom  $\mathbb{Z}$  of the one-dimensional electron gas via

$$\kappa = 1 + 2/\mathbb{Z}. \quad (2b)$$

Moreover, the degrees of freedom  $\mathbb{Z}$  depend on  $T_{e,0}$  through

$$\mathbb{Z}(\beta) = 2 \left[ 1 + \beta \left( \frac{K_0(\beta)}{K_1(\beta)} - 1 \right) \right], \quad (2c)$$

with  $\beta = m_e c^2 / T_{e,0}$  and  $K_n$  being the modified Bessel functions of second kind and  $n$ -th order. They increase from  $\mathbb{Z} = 1$  to  $\mathbb{Z} = 2$  with rising temperature from  $T_{e,0} \ll m_e c^2$  (nonrelativistic case) to  $T_{e,0} \rightarrow \infty$  (ultrarelativistic case). At the same time, the adiabatic index is decreasing from  $\kappa = 3$  to  $\kappa = 2$ . Thus, from a practical point of view, only the domain  $2 \leq \kappa \leq 3$  turns out to be important for our studies, especially in the Secs. IV and V. However, up to that point we want to keep the analytic results as general as possible, assuming the weaker limitation,<sup>4</sup>  $\kappa \geq 1$ .

The relation (2a) was initially derived using a fluid description of the electron gas. It has been used to study the expansion of a plasma under the approximation of quasineutrality and wave-breaking effects from a target with an initial density gradient [62] as well as to determine the optimal thickness of an ultra-thin target in the TNSA process [63,64]. Although the treatment of the hot electrons in our study is always based on a kinetic description, we will consider the relations (2a)–(2c)—according to the original context—as the *hydrodynamic approach*.

Besides the form of the initial electron distribution function, our model has much in common with the analysis of Ref. [39] and followers. This means that the electric potential  $\phi$  is determined by the (nonlinear) Poisson equation

$$\varepsilon_0 \frac{\partial^2 \phi(x,t)}{\partial x^2} = e[n_e(\phi(x,t)) - Z_i n_i(x,t)], \quad (2d)$$

depending on the space coordinate  $x$  and time  $t$ . The charge number of the ions is set to be  $Z_i$  and their initial spatial density  $n_i$  is given as a steplike function,

$$n_i(x,t=0) = n_{i,0} \Theta(-x), \quad (2e)$$

with the Heaviside-Theta function  $\Theta(x)$ . Furthermore, we set  $n_{e,0} = Z_i n_{i,0}$ . To close the system of equations, it is necessary to describe the ion motion. This will be done using the hydrodynamic equations for a perfect fluid,

$$\frac{\partial n_i}{\partial t} + \frac{\partial}{\partial x}(n_i v_i) = 0, \quad (2f)$$

$$\frac{\partial v_i}{\partial t} + v_i \frac{\partial v_i}{\partial x} = -\frac{Z_i e}{m_i} \frac{\partial \phi}{\partial x}, \quad (2g)$$

which are valid as long as  $v_i(x)$  is a single-valued function, meaning that the ions do not overtake each other.

The paper is organized as follows. In Sec. II we are going to derive analytic expressions for the motion of the ion front. Section III contains a short recall of Mora’s theory

<sup>4</sup>The case  $\kappa = 1$ , which corresponds to the isothermal situation, has to be understood as a limiting process,  $\kappa \rightarrow 1$ .

[57], which studies the adiabatic plasma expansion assuming Maxwellian hot electrons with decreasing temperature (adiabatic Maxwellian expansion). Here, we add some further analytical results. Afterwards, the findings described in Secs. II and III are compared with each other in Sec. IV. Finally, we discuss various proton-ion acceleration experiments in Sec. V, employing the models specified before. Section VI contains the concluding remarks.

## II. ANALYTICS FOR STEPLIKE DISTRIBUTED ELECTRONS

Following Ref. [65] one can derive a self-similar solution for the system (2) under the assumption of charge quasineutrality,<sup>5</sup>  $n_e = Z_i n_i$ . It takes the form

$$\phi_{ss} = \frac{T_{e,0}}{e} \left[ \frac{\kappa - 1}{(\kappa + 1)^2} \left( \frac{x}{c_s t} \right)^2 - \frac{4\sqrt{\kappa}}{(\kappa + 1)^2} \frac{x}{c_s t} - \frac{\kappa(\kappa + 3)}{(\kappa + 1)^2} \right], \quad (3a)$$

$$v_{i,ss} = \frac{2c_s}{1 + \kappa} \left( \frac{x}{c_s t} + \sqrt{\kappa} \right), \quad (3b)$$

$$Z_i n_{i,ss} = n_{e,0} \left[ \frac{2}{\kappa + 1} \left( 1 - \frac{\kappa - 1}{2\sqrt{\kappa}} \frac{x}{c_s t} \right) \right]^{2/(\kappa - 1)}, \quad (3c)$$

with the ion-acoustic velocity  $c_s = \sqrt{Z_i T_{e,0}/m_i}$ . Note that equations (3) are identical with the self-similar result of Ref. [62]. Considering the self-similar solution (3) mathematically, it is valid in the domain<sup>6</sup>  $-\sqrt{\kappa} < x/c_s t \leq 2\sqrt{\kappa}/(\kappa - 1)$ , i.e., within a region where the condition of charge neutrality is sufficiently fulfilled.<sup>7</sup> In case of an ion distribution with strong spatial variations this condition is violated, because the electron distribution cannot follow these variations instantaneously due to the thermal smoothing of the electron density. Hence, the self-similar solution is not suitable as a model for the expansion of a target with an initially steplike density profile at the very beginning of the acceleration process. At later times, however, when the ion density profile smooths out due to the expansion itself, the relations (3) provide a good approximation to the exact solution of the system (2) within the quasineutral region (see Fig. 1).

While the lower boundary of that quasineutral region is approximately given by the position of the rarefaction wave  $-\sqrt{\kappa} c_s t$ , which is identical with the lower boundary of

<sup>5</sup>Note the different meaning of the quasineutral condition  $n_e = Z_i n_i$  and the assumption  $n_{e,0} = Z_i n_{i,0}$  made before. While the latter is just a special choice for the factor in the electron density function  $n_e$ , the former is a relation between the functions  $n_i$  and  $n_e$  in a certain domain of  $x$ .

<sup>6</sup>For  $x > 2\sqrt{\kappa} c_s t/(\kappa - 1)$  the solution is continued by  $e\phi_{ss} \equiv -\kappa T_{e,0}/(\kappa - 1)$  and  $n_{i,ss} \equiv 0$ . Here the ion velocity  $v_{i,ss}$  is not defined due to the absence of ions. Moreover, for  $x < -\sqrt{\kappa} c_s t$ , the expressions (3) become meaningless. Instead, one has  $v_i \equiv 0$ ,  $n_i \equiv n_{e,0}/Z_i$ , and  $\phi_{ss} \equiv 0$ .

<sup>7</sup>Strictly spoken, in a general situation the quasineutrality condition is a necessary but not a sufficient condition. However, with respect to the problem discussed here, one may regard it as a sufficient condition, too.

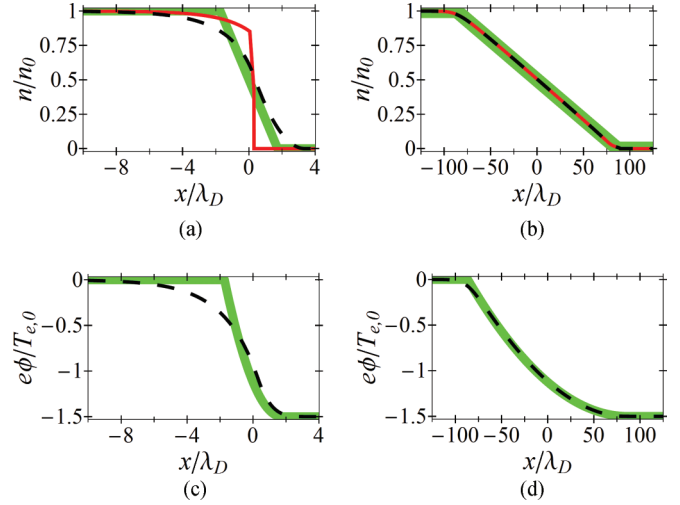


FIG. 1. (Color online) Illustration of the self-similar solution (3) for  $\kappa = 3$  in comparison with the numerical solution of the equations (2). Panels (a) and (b) show the spatial density distributions of the particles at the instants  $\omega_{pi} t = 1$  and  $\omega_{pi} t = 50$ , respectively. The dashed black and the solid red (gray) curves correspond to the exact electron and ion densities, respectively, obtained by solving Eqs. (2) numerically, whereas the thick green (light gray) lines represent the self-similar solution (3c). Note that  $Z_i = 1$  is assumed in the plotted example. In panels (c) and (d), the exact electric potential evaluated numerically from Eqs. (2) (dashed black line) is compared with the self-similar relation (3a) [thick green (light gray) curve] for  $\omega_{pi} t = 1$  and  $\omega_{pi} t = 50$ , respectively.

the range of validity of Eqs. (3), the upper boundary of the quasineutral region does not equal the upper boundary  $2c_s t\sqrt{\kappa}/(\kappa - 1)$  of the self-similar solution (3). Instead, it is approximately given by the point where the local electron Debye length,  $\lambda_{D,local} = \sqrt{\epsilon_0 T_{e,0}/(n_e(x) e^2)}$ , exceeds the scale length  $l_{ss}$  of the spatial variation in the ion density (see Refs. [41,46]). By evaluating the local scale length  $l_{ss} = |n_i/(\partial n_i/\partial x)|$  of the self-similar ion density (3c) at the initial target boundary ( $x = 0$ ), which we take as a representative position, one finds  $l_{ss} = \sqrt{\kappa} c_s t$ . Consequently,  $\lambda_{D,local}$  exceeds  $l_{ss}$  at the position

$$x_{f,ss} = \frac{2\sqrt{\kappa}}{\kappa - 1} c_s t \left[ 1 - \frac{\kappa + 1}{2} (\sqrt{\kappa} \omega_{pi} t)^{1-\kappa} \right]. \quad (4)$$

Here,  $\omega_{pi} = \sqrt{Z_i n_{e,0} e^2/(m_i \epsilon_0)}$  denotes the ion plasma frequency.

From a physics point of view, Eq. (4) is an approximative expression for the position of the ion front, because the quasineutral condition fails here as a result of the jump discontinuity in the ion density, which the electron density cannot follow directly. According to the self-similar solution, the ion velocity at the position  $x_{f,ss}$  is given by

$$v_{f,ss} = 2c_s \frac{\sqrt{\kappa}}{\kappa - 1} [1 - (\sqrt{\kappa} \omega_{pi} t)^{1-\kappa}]. \quad (5)$$

Note, that Eq. (5) at  $t \rightarrow \infty$  equals the velocity at which the upper boundary of the range of validity of the self-similar solution is propagating. In addition, Eq. (5) is consistent with the expression given by Mora [41] for  $\kappa \rightarrow 1$ . By taking the derivative of Eq. (5) we deduce the corresponding scaling of

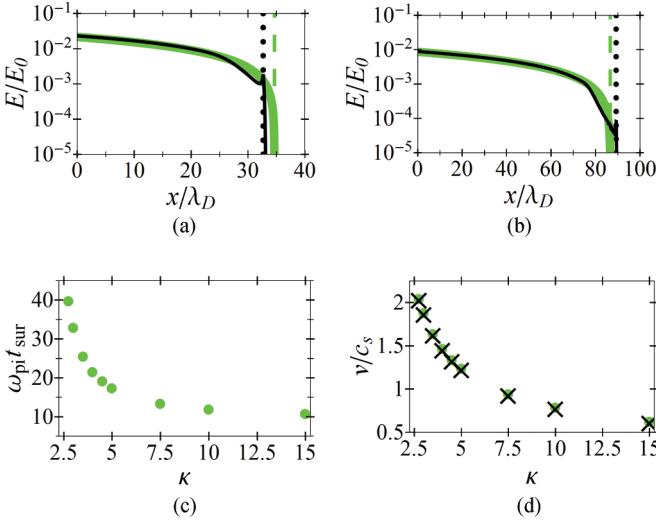


FIG. 2. (Color online) Panels (a) and (b) illustrate the self-similar electric field [thick green (light gray) curve] in comparison with simulation results (black curve) for  $\kappa = 3$  at the instants  $\omega_{pi} t = 20$  and  $\omega_{pi} t = 50$ , respectively. The ion front—marked by the dotted black vertical line—surpasses the upper boundary  $2c_s t \sqrt{\kappa}/(\kappa - 1)$  of the self-similar solution [dashed green (light gray) vertical line] at some instant  $\omega_{pi} t_{sur}$  between 20 and 50. As exhibited in (c), such a point  $\omega_{pi} t_{sur}$  exists for each value of  $\kappa$ . Consequently, the final velocity of the ion front  $v_{max}$  [see Eq. (12) below] always exceeds the velocity  $2c_s \sqrt{\kappa}/(\kappa - 1)$ , at which the upper boundary of the self-similar solution is propagating. Plot (d) shows the velocity of the ion front at the instants of surpassing [green (light gray) dots] against the final velocity of the ion front (black crosses) for different  $\kappa$ . Both velocities differ by less than 1%.

the electric field strength at the ion front as

$$E_{f,ss}(t) \propto t^{-\kappa}. \quad (6)$$

Although the self-similar solution is useful for the investigation of the general properties of the plasma expansion, it does not allow for a characterization of the complete process. First, it cannot specify the expansion in the early stages due to the considerable violation of quasineutrality. Moreover, even for later times, this condition fails at the ion front. Consequently, the self-similar solution does not provide a precise deduction of the electric field strength at the ion front. In case of isothermal electrons,  $\kappa \rightarrow 1$ , Mora circumvented this difficulty by utilizing numerical results implying that the electric field  $E(t)$  at the ion front for  $\omega_{pi} t \gg 1$  is approximately twice the value  $E_{f,ss}(t)$  given by the self-similar solution [41]. But for parameters  $\kappa \neq 1$ , simulations show that the ion front surpasses the upper boundary of the self-similar solution,  $2c_s t \sqrt{\kappa}/(\kappa + 1)$ , at some instant (see Fig. 2). Hence, the self-similar solution (3) cannot formally be used to characterize the motion of the ion front at later times.

However, simulations<sup>8</sup> reveal saturation in the growth of the ion front velocity when approaching this moment of

surpassing, as it becomes clear from Fig. 2(d). Hence, the self-similar description of the electric field strength at the ion front beyond the point of surpassing does not introduce an essential error. Therefore, we may reason that the scaling of the electric field predicted by the self-similar solution (6) approximates the evolution of the electric field at the ion front for late times  $\omega_{pi} t \gg 1$  sufficiently well, despite the restriction mentioned above.

In order to express the electric field at all instants of time, we propose—analogously with the isothermal fit in Ref. [41]—the generalized expression

$$E(t) \approx \frac{E(t=0)}{[1 + C(\kappa)(\omega_{pi} t)^2]^{\kappa/2}}, \quad (7)$$

which obeys the asymptotic behavior (6). Here,  $C(\kappa)$  is a function of  $\kappa$  only and  $E(t=0)$  denotes the initial field strength at the ion front. The latter value can be determined by integration of Eq. (2d) with the electron density (2a), resulting in

$$E(t=0) = \sqrt{2} \kappa^{-\frac{\kappa}{2(\kappa-1)}} E_0, \quad (8)$$

where  $E_0 = \sqrt{n_{e,0} T_{e,0}/\epsilon_0}$ . For values  $\kappa \lesssim 10$ , the expression (7) properly fits the simulation results, as long as  $C(\kappa)$  is well chosen. This is demonstrated in Fig. 3(a) for three values of  $\kappa$ . Since relation (7) is a heuristic fit,  $C(\kappa)$  cannot be determined unambiguously. However, a comparison with the best-fit values  $C_n = C(\kappa_n)$  gained from a series of simulations with various values  $\kappa_n$  shows that

$$C(\kappa) = \frac{1}{2} \frac{1}{\exp(1) + \kappa - 1} \quad (9)$$

is a good approximation, as illustrated in Fig. 3(b). Furthermore, expression (7) together with Eq. (9) leads to the fit formula found by Mora for the case  $\kappa = 1$ .

Using the empiric fit (7), we obtain the velocity,

$$\frac{v(t)}{c_s} = \sqrt{2} \kappa^{-\frac{\kappa}{2(\kappa-1)}} \omega_{pi} t {}_2F_1 \left[ \frac{1}{2}, \frac{\kappa}{2}; \frac{3}{2}; -C(\kappa)(\omega_{pi} t)^2 \right], \quad (10)$$

as well as the position of the ion front,

$$\frac{x(t)}{\lambda_D} = \sqrt{2} \kappa^{-\frac{\kappa}{2(\kappa-1)}} \left\{ \frac{[1 + C(\kappa)(\omega_{pi} t)^2]^{1-\frac{\kappa}{2}} - 1}{C(\kappa)(\kappa - 2)} + (\omega_{pi} t)^2 {}_2F_1 \left[ \frac{1}{2}, \frac{\kappa}{2}; \frac{3}{2}; -C(\kappa)(\omega_{pi} t)^2 \right] \right\}, \quad (11)$$

as functions of time. Here,  ${}_2F_1$  denotes the Gaussian hypergeometric function and  $\lambda_D = \sqrt{\epsilon_0 T_{e,0}/(n_{e,0} e^2)}$  is the electron Debye length. Relations (10) and (11) are displayed in Fig. 3(c) and 3(d) and reproduce the simulation data well. The fit precision decreases slightly with increasing  $\kappa$ . However, for

to a PIC code—to solve the ions' equations of motion (2f) and (2g). Moreover, it can handle different approximations for the evolution of the electron phase-space density, as described in Sec. IV. The code, which was already used in a previous study [61], is quite similar to a number of codes used in several studies (e.g., Refs. [41,43,57,66–69]) and was carefully tested against those published results.

<sup>8</sup>The simulations in this article were performed with a code which solves the system (2) numerically. Primarily, it consists of a solver for the nonlinear Poisson equation (2d) and a particle stepper—similar

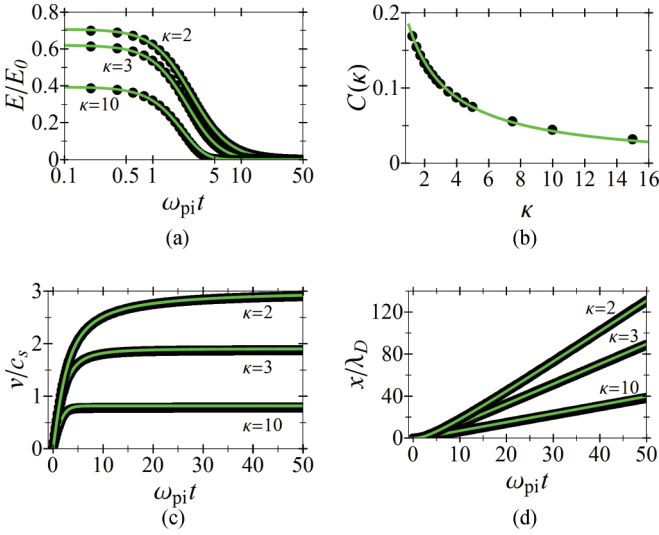


FIG. 3. (Color online) In (a), the electric field strength at the ion front in units of  $E_0$  as a function of time is shown for  $\kappa = 2, 3$ , and  $10$ . Black dots correspond to simulation results, while the green (light gray) curves represent the analytical estimate (7). Panel (b) displays the best-fit values for  $C(\kappa)$  found by simulations (black dots) in comparison with Eq. (9) [green (light gray) curve]. In (c) and (d), the time dependence of the normalized ion front velocity and its position are plotted, respectively. The corresponding estimates (10) and (11) are depicted by green (light gray) lines; black dots show the results of simulations.

values  $\kappa \leq 3$  the relative error in  $v(t)$  is still less than 1% for all times  $t$ .

From relation (10), we deduce the maximum ion velocity in the limit  $t \rightarrow \infty$  as

$$v_{\max}/c_s = \sqrt{2\chi(\kappa)}. \quad (12)$$

The function  $\chi(\kappa)$  depends on  $\kappa$  only and is defined as

$$\chi(\kappa) = 4\pi \frac{\Gamma\left[\frac{\kappa+3}{2}\right]^2}{\Gamma\left[\frac{\kappa}{2}\right]^2} \frac{\kappa^{-\frac{\kappa}{\kappa-1}}}{C(\kappa)(\kappa^2-1)^2}. \quad (13)$$

From (13) it is evident, that the final maximum ion velocity is finite for  $\kappa > 1$ , in contrast to the isothermal case ( $\kappa \rightarrow 1$ ). This is not surprising, since the steplike electron energy distribution does have a finite cut-off energy (see Ref. [61]). As a consequence, the difference of the potential values at  $x = -\infty$  (deep inside the target) and  $x = \infty$  (in vacuum) is finite and, hence, the maximum kinetic energy a test particle can gain is limited, too. The correlation between a finite cut-off electron energy and the limitation of the final maximum ion energy has been studied in the case of a truncated Maxwellian distribution for (i) the free expansion of a plasma consisting of one ion species [46,47] and (ii) the acceleration of light ions, which were assumed as test particles in the field of immobile heavy ions [48,49,51].

It is interesting to note that the maximum velocity (12) is close to the velocity  $2c_s \sqrt{\kappa}/(\kappa-1)$  of the upper boundary of the self-similar solution (3). Indeed, the relative difference between both terms is less than 15% for all  $\kappa \leq 10$ . Furthermore, from Eq. (12) we can derive the maximum ion energy

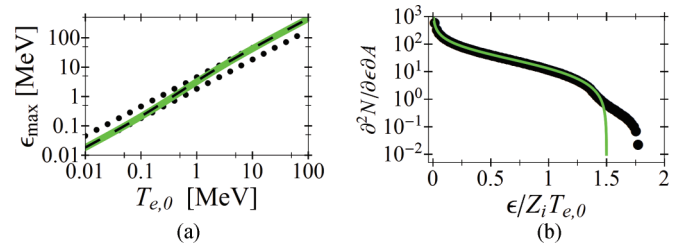


FIG. 4. (Color online) Panel (a) displays the maximum energy per charge number of the accelerated ions as a function of the initial electron energy. The bold green (light gray) curve corresponds to Eq. (14) with  $\kappa$  expressed as function of the electron temperature  $T_{e,0}$  by applying the relation  $\kappa = 1 + 2/Z$  and Eq. (2c). That exact curve is almost perfectly covered by the approximation (15) (dashed black curve). In addition, the minorant and majorant functions (16) are displayed by dotted black lines. Panel (b) shows the energy spectrum for  $\kappa = 3$  at  $\omega_{pi} t = 50$ . The black dots correspond to the results of a simulation, while the green (light gray) curve is determined by Eq. (17). Here, the number of ions per unit surface and unit energy is normalized to  $n_{i,0} \lambda_D / Z_i T_{e,0}$ .

per charge number:

$$\epsilon_{\max}/Z_i = T_{e,0} \chi(\kappa). \quad (14)$$

Substituting  $\kappa$  by the number of degrees of freedom  $Z$  via Eq. (2b) and expressing this parameter in terms of the initial electron temperature  $T_{e,0}$  by using Eq. (2c), the relation (14) will depend on  $T_{e,0}$  only. For practical use, we give an approximative expression (see also Fig. 4):

$$\epsilon_{\max}/Z_i \approx T_{e,0} \frac{1.36312 + 4.58725 T_{e,0}/\text{MeV}}{0.750591 + T_{e,0}/\text{MeV}}. \quad (15)$$

From this relation one can extract the minorant and majorant functions,

$$1.82 T_{e,0} \leq \epsilon_{\max}/Z_i \leq 4.59 T_{e,0}. \quad (16)$$

Finally, the number of ions per unit energy and unit surface (energy spectrum) can be approximately calculated from the self-similar solution (3) as

$$\frac{\partial^2 N}{\partial \epsilon \partial A} = \frac{\kappa+1}{2^{3/2}} \frac{n_{i,0} c_s t}{\sqrt{Z_i T_{e,0}} \epsilon} \left(1 - \frac{\kappa-1}{\sqrt{2\kappa}} \sqrt{\frac{\epsilon}{Z_i T_{e,0}}}\right)^{\frac{2}{\kappa-1}}. \quad (17)$$

In the limit  $\kappa \rightarrow 1$ , this relation reproduces the result given in Ref. [41].

### III. ADIABATIC EXPANSION WITH MAXWELLIAN ELECTRONS

Because of the energy conservation in the plasma expansion with a single steplike hot electron distribution, the model presented in Sec. II offers an appropriate framework to describe the adiabatic expansion of a plasma slab into vacuum. However, there are other expansion models, which ensure the energy conservation as well.

One well-known approach is the so-called *adiabatic Maxwellian model* studied in Ref. [57]. In contrast to the hydrodynamic model it is based on a Maxwell-Jüttner electron distribution, implying a hot electron density relation of the

form

$$n_e(\phi) = n_{e,0} \exp\left(\frac{e\phi}{T_e}\right). \quad (18)$$

In the adiabatic Maxwellian model, the electron temperature  $T_e$  is assumed to be time dependent,  $T_e = T_e(t)$ . Here, the electron energy is varied in such a way that the conservation of the total energy of the system is ensured.

In this section we are going to recall and partially extend the results of Ref. [57]. This will serve—together with the findings of Sec. II—as the basis for further discussion in the following sections. Here, we will follow an empirical line of thinking and we will focus on a few essential points. A more general theoretical treatment of an adiabatic Maxwellian expansion is, for example, given by Kovalev *et al.* (e.g., Refs. [52,53]).

According to Ref. [41], the electric field at the ion front of an expanding plasma driven by isothermal Maxwellian electrons is given by

$$E(t) = \frac{E(t=0)}{\sqrt{1+\tau^2}}, \quad (19)$$

with  $\tau = \omega_{pi} t / \sqrt{2 \exp(1)}$ . Here, the ions are initially contained in a semi-infinite slab (steplike target), as described by Eq. (2e). For  $t \rightarrow \infty$ , Eq. (19) predicts the behavior  $E(t) \propto t^{-1}$ , in agreement with the self-similar solution (see, e.g., Refs. [39,65]). In accordance with the unlimited amount of initial total energy, the expansion of the plasma slab proceeds isothermally.

If the plasma slab has initially a finite extension<sup>9</sup>  $L$ , the ion density may be written in the form

$$n_i(x, t=0) = n_{i,0} \Theta(L - 2|x|). \quad (20)$$

For the adiabatic process [57], one finds the dependencies  $T_e \propto t^{-2}$  by starting from nonrelativistic temperatures  $T_{e,0}$  as well as  $T_e \propto t^{-1}$  in the ultrarelativistic case with  $T_{e,0} \gg m_e c^2$ . These time scalings for the hot electron temperature induce the corresponding field dependencies  $E(t) \propto t^{-2}$  for nonrelativistic and  $E(t) \propto t^{-3/2}$  for ultrarelativistic plasmas.

At nonrelativistic electron energies, a simple expression for the electric field at the ion front, which guarantees the correct asymptotic temporal behavior, is assumed in analogy with Eq. (19) as

$$E(t) = \frac{E(t=0)}{\sqrt{1+\alpha\tau^2+\beta\tau^4}}. \quad (21)$$

<sup>9</sup>In order to avoid misunderstandings, which may appear in the context of the terms *semi-infinite/finite plasma slab* and *unlimited/limited large amount of energy*, we want to specify these terms. As a direct consequence of the one-dimensional modeling, the initial ion distribution is always infinitely extended in the transverse  $y$  and  $z$  directions. Therefore, the total number of ions and electrons contained in the plasma is always infinitely large, leading to an unlimited amount of initial energy, too. However, this is not crucial for the model and the evolution of the electron temperature, since the essential quantity here is the total initial energy per area  $dydz$  contained in the system,  $\partial^2 \varepsilon / \partial y \partial z = \int_{\mathbb{R}} \partial^3 \varepsilon / \partial y \partial z \partial x dx$ . For finite values of the initial energy per area the plasma expansion proceeds adiabatically, otherwise isothermally. Note that for practical reasons we shorten the term *energy per area* simply to *energy*.

Here,  $\alpha$  and  $\beta$  are functions of the normalized initial target thickness,  $L/\lambda_D$ , only. By demanding  $\alpha(L/\lambda_D) = 1$  and  $\beta(L/\lambda_D) = 0$  for  $L/\lambda_D \rightarrow \infty$ , the ansatz (21) includes the isothermal limit by letting the initial thickness of the target go towards infinity. Numerous simulations have shown that Eq. (21) works well for targets with  $L/\lambda_D \gtrsim 0.5$ .

For ultrarelativistic hot electrons we should use the corresponding relation

$$E(t) = \frac{E(t=0)}{\sqrt{1+\gamma\tau^2+\delta\tau^3}}, \quad (22)$$

with  $\gamma$  and  $\delta$  again being functions of  $L/\lambda_D$  only. However, we will restrict the further discussion to the nonrelativistic case. Asking about the influence of this restriction on the maximum attainable ion velocity, we obtain variations in this quantity of less than 10% for  $L/\lambda_D \gtrsim 0.5$  in the time domain  $\omega_{pi} t \lesssim 25$ , which is typical for many related experiments. This spread is tolerable for the analysis in the next sections, where we are interested in general relations and scaling laws.

The unknown functions  $\alpha$  and  $\beta$  were specified in a series of simulations varying the normalized initial target thickness  $l = L/\lambda_D$ . Starting from the fit values  $\alpha_n = \alpha(l_n)$  and  $\beta_n = \beta(l_n)$  determined from the simulations, we found the following empirical relations:

$$\alpha = \frac{\chi_1 l^{3/2} + \chi_2 l^2 + \chi_3 l^{5/2} + \chi_4 l^3}{1 + \chi_5 l^{3/2} + \chi_6 l^2 + \chi_7 l^{5/2} + \chi_4 l^3}, \quad (23a)$$

$$\beta = \left( \frac{\eta_1 l + \eta_2 l^{3/2} + \eta_3 l^2}{1 + \eta_4 l^{1/2} + \eta_5 l^2 + \eta_6 l^{7/3}} \right)^4,$$

with the coefficients

$$\begin{aligned} (\chi_j) &= (-0.0129981, 0.525472, -0.144767, 0.0325432, \\ &\quad -0.70989, 0.860559, -0.199045), \\ (\eta_j) &= (0.0926025, 5.65707, 0.2323, 12.9501, \\ &\quad 2.09728, 0.0701358). \end{aligned} \quad (23b)$$

The fits (23) obey the required conditions  $\alpha(l) = 1$  and  $\beta(l) = 0$  in the limit  $l \rightarrow \infty$  and they reproduce the values  $\alpha_n$  and  $\beta_n$  quite well within the range  $0.5 \lambda_D \leq L \leq 500 \lambda_D$ , as shown in Fig. 5.

An approximate expression for the electric field strength  $E(t=0)$  can be found by making a quadratic ansatz for the potential inside the target,  $\phi(x) = \phi(0) + \phi''(0)x^2/2$ , and substituting it in the first integral of the Poisson equation (2d). One obtains the expression

$$\sigma(l) = \sqrt{\frac{2}{\exp(1)}} \sqrt{\frac{l^2}{8+l^2}} \exp\left(\frac{8}{8+l^2}\right) \quad (24)$$

for the normalized initial field strength at the target boundary,  $\sigma = E(t=0)/E_0$ . Although the quadratic ansatz for the potential is, strictly speaking, valid for thin targets only, Eq. (24) seems to be an excellent approximation for targets of arbitrary thickness, as one can see from Fig. 5(c).

Using the relations (23) and (24) in Eq. (21), the deviation  $|E(t) - E_{\text{num}}(t)|/E_0$  of the ansatz (21) compared to the simulation values  $E_{\text{num}}(t)$  is less than 1% for  $0.5 \lambda_D \leq L \leq 500 \lambda_D$  [see, for example, Figs. 6(a) and 6(b)]. The integration

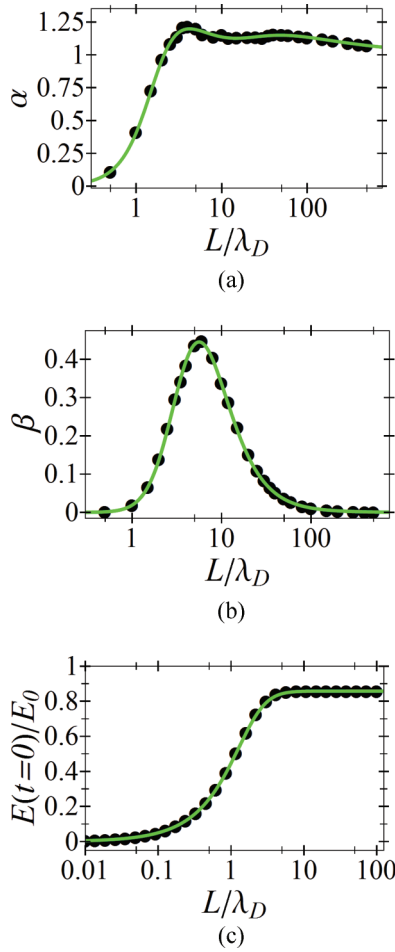


FIG. 5. (Color online) Panels (a) and (b) show the best fit values for  $\alpha_n$  and  $\beta_n$  (black dots) determined by simulations of targets with different thicknesses  $L_n$  in comparison with the empirical fit functions (23), depicted by green (light gray) curves. In panel (c), the expression (24) for the normalized initial field strength [green (light gray) curve] is plotted together with the simulation values  $\sigma_n$  (black dots).

of Eq. (21) yields expressions for the ion velocity

$$\frac{v(t)}{c_s} = \sqrt{2 \exp(1)} \frac{\sigma}{\sqrt{-a}} F \left[ \arcsin(\sqrt{-a} \tau) \middle| \frac{b}{a} \right], \quad (25)$$

and for the position of the ion front,

$$\frac{x(t)}{\lambda_D} = 2 \exp(1) \sigma \left( \frac{\tau}{\sqrt{-a}} F \left[ \arcsin(\sqrt{-a} \tau) \middle| \frac{b}{a} \right] - \frac{1}{\sqrt{ab}} \ln \left[ \frac{\sqrt{b} \sqrt{1+a\tau^2} + \sqrt{a} \sqrt{1+b\tau^2}}{\sqrt{a} + \sqrt{b}} \right] \right) \quad (26)$$

as functions of time. Here,  $F$  is the incomplete elliptic integral of the first kind and the coefficients  $a$  and  $b$  are given by  $(\alpha \mp \sqrt{\alpha^2 - 4\beta})/2$ . The functions (25) and (26) are plotted in Fig. 6 for the cases  $L/\lambda_D = 1$  and  $L/\lambda_D = 100$ .

In addition, from Eq. (25) one can directly calculate the kinetic energy of the ions at the front as a function of time. By letting  $t \rightarrow \infty$ , one gets the maximum energy of the ions,

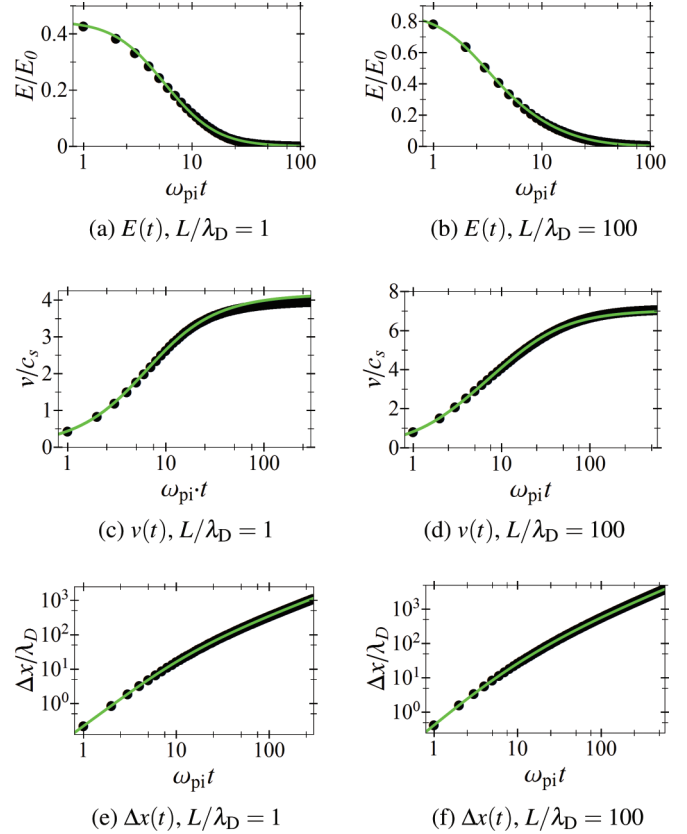


FIG. 6. (Color online) In panels (a), (b), and (e), the evolution of the electric field strength at the ion front as well as the velocity and the extension of the ion front are shown for a normalized initial target thickness  $L/\lambda_D = 1$ , respectively. The right column of panels depicts the same results for  $L/\lambda_D = 100$ . Black dots represent the simulation results, while the green (light gray) lines correspond to the analytic estimates, Eqs. (21), (25), and (26), respectively. Obviously, the analytic results fit the numerical data quite well for the plotted examples  $L/\lambda_D = 1$  and  $L/\lambda_D = 100$ . For intermediate values  $L/\lambda_D$  we observed a similar coincidence.

given by

$$\varepsilon_{\max}/Z_i = T_{e,0} \exp(1) \frac{\sigma^2}{a} K \left[ 1 - \frac{b}{a} \right]^2. \quad (27)$$

Here,  $K$  denotes the complete elliptic integral of the first kind. The energy relation (27) will be used in the following sections and is displayed in Figs. 8(a) and 13.

#### IV. COMPARISON OF THE ADIABATIC MODELS

Before we compare the results obtained from the hydrodynamic model, which implies a single steplike hot electron distribution function, with models assuming Maxwellian hot electrons, we recall some characteristic properties of the different approaches.

All models treat the electrons in a stationary approximation, as described in Sec. I. This ansatz offers a simple framework for the electrons at any moment in time. However, since one operates with the stationary Vlasov equation, the temporal evolution of the electron distribution is not intrinsically specified.

To compensate for this drawback, additional assumptions are needed.

Concerning Maxwellian electrons, the following approaches have been investigated. In the *isothermal Maxwellian model* the same distribution function  $f_{e,0}$  (a Maxwell-Jüttner distribution) is used at each instant of time. The second approach—the *adiabatic Maxwellian model*—was already discussed in Sec. III. In contrast to the isothermal Maxwellian model, one introduces small changes of  $f_{e,0}$  with time in a heuristic manner, as described in Ref. [57], for example. Using this approach one retains a Maxwell-Jüttner distribution for the function  $f_{e,0}$  at each instant but modifies the electron temperature with time,  $T_e = T_e(t)$ . The evolution of  $T_e(t)$  must be determined in such a way that the total energy of the system is always conserved. The third approach treats the electron cooling in a more sophisticated way [67,68]. We keep in mind that the initial distribution function describes an ensemble of many electrons with different energies. Those individual electrons are oscillating in the electric potential around the ions. As long as the ions are immobile the electric potential is conservative and, therefore, the total energy of each individual electron as well as the function  $f_{e,0}$  are conserved over time. However, as soon as the ions start to move, the electric potential slightly changes with time. Therefore, the motion of the electrons is no longer conservative, their total energy and, consequently, their distribution function will change with time, since energy is transferred to the ions. Assuming that the variation of the ion configuration is not too fast,<sup>10</sup> a fully dynamic modeling of the electrons on the basis of adiabatic invariants may be accomplished [67]. We refer to this ansatz as the *kinetic model*. It is generally suitable for an arbitrary initial distribution function  $f_{e,0}$ . Hence, it also allows us to describe the evolution of the non-Maxwellian electron distribution implied by the hydrodynamic approach. In case of an initially Maxwellian electron distribution we refer to it as the *kinetic Maxwellian model*.

As a result of the kinetic modeling, an initially Maxwellian energy distribution  $f_{e,0}$  in general evolves into a non-Maxwellian distribution at later times, see, e.g., Refs. [67,68]. Asking for the evolution of the electron distribution in the hydrodynamic approach, one has to note that the kinetic approach preserves the implied initial steplike electron distribution  $f_{e,0}$ , as shown in Ref. [61]. Therefore, the hydrodynamic approach (2a)–(2c) describes the electron evolution in a correct way (in the sense of the kinetic model).

To conclude this discussion, we note two general differences in the quoted models: (i) by the specific choice of the initial electron energy distribution  $f_{e,0}$  and (ii) in the way how the temporal evolution of this specific function  $f_{e,0}$  is determined. In the following, we want to compare

<sup>10</sup>According to Ref. [67], the necessary condition can be expressed as  $\mathcal{T}_e/t_\phi \ll 1$ , with  $\mathcal{T}_e$  being the period of motion of an electron with energy  $\varepsilon$  and  $t_\phi$  denoting the characteristic time of variations in the potential “seen” by the electron. This time on its part may be determined by the ratio of the electron energy and the mean variation of the potential during a period of the electron motion, that is,  $\varepsilon / \langle \frac{\partial \phi}{\partial t} \rangle$ . In order to guarantee the equivalence, the condition  $\mathcal{T}_e/t_\phi \ll 1$  has to be fulfilled for all electrons.

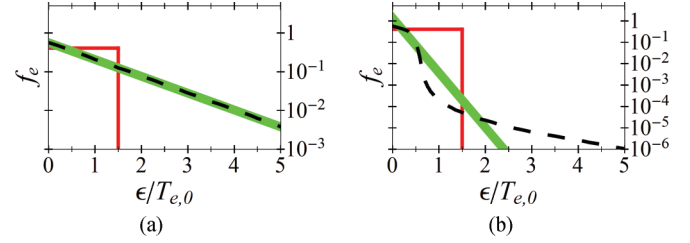


FIG. 7. (Color online) Panels (a) and (b) illustrate the different electron distributions underlying the different models (nonrelativistic case) for a target with an initial thickness  $L/\lambda_D = 80$  at  $\omega_{pi} t = 0$  and  $\omega_{pi} t = 50$ , respectively. While Ref. [57] is based on Maxwell-like distributed electrons [dashed black and bold green (light gray) curves], the hydrodynamic approach used here implicitly assumes a steplike distribution [solid red (gray) line], see Ref. [61]. The green (light gray) lines correspond to the adiabatic Maxwellian case, whereas the dashed black curves show the changing electron distribution function in the kinetic Maxwellian model. Here,  $f_e$  is normalized to  $n_{e,0}/\sqrt{2m_e T_{e,0}}$ .

the hydrodynamic approach with the adiabatic Maxwellian model [57] and with the kinetic Maxwellian model [67]. All these approaches conserve the total energy of the system and are, therefore, suitable for the description of an adiabatic plasma expansion. Because of the complex interplay between the expansion and the electron cooling, however, this task is complicated within the Maxwellian models.

The various electron distributions, which are illustrated in Fig. 7, lead to different behavior during the ion acceleration process. While no finite velocity for the ion front exists in the case of Maxwell-distributed electrons and half-infinite plasma slabs, we identify the limit (12) for a steplike electron energy distribution. In order to get finite ion energies in the case of Maxwellian electrons, one has to operate with foils (targets of limited thickness). This leads to different final ion energies in dependence on the target thickness, as shown in Fig. 8(a). In contrast, in the hydrodynamic approach, the final maximum energy of the ions quickly saturates for an increasing thickness of the foil, as also illustrated in Fig. 8(a). Moreover, these values are lower by almost one order of magnitude for foil thicknesses  $L$  in the range of  $\lambda_D \leq L \leq 100\lambda_D$ , as compared with the results assuming Maxwellian hot electrons.

The final energy in the case of nonrelativistic Maxwell-like electrons is given by Eq. (27), which is approximately equal to  $\varepsilon_{\max}/Z_i = 2 T_{e,0} \ln(0.32 L/\lambda_D + 4.2)^2$  for  $L/\lambda_D \geq 20$ , see Ref. [57]. This expression depends on  $T_{e,0}$  as well as on  $n_{e,0}$  (through  $\lambda_D$ ), whereas the relation (14) of the hydrodynamic model is only a function of the electron temperature  $T_{e,0}$ .

To give an explanation for the remarkable difference in the final maximum ion energies, predicted by the Maxwellian and the hydrodynamic approaches, we may exclude differences in the initial electric field strength as an essential reason, because the ratio  $E_{\text{Maxwell}}(t=0)/E_{\text{hydro}}(t=0)$  is given by  $\sqrt{\kappa^{\kappa/(\kappa-1)}/\exp(1)}$ , which is smaller than 1.4 for arbitrary values of  $T_{e,0}$ . Furthermore, the total energy of the system (initial electric field energy plus initial thermal energy of the electrons) does not significantly differ for foils with a thickness greater than or equal to a few Debye lengths [see Fig. 8(b)].

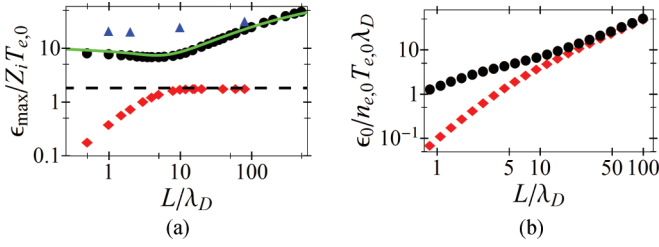


FIG. 8. (Color online) In (a) the final maximum energy of the ions as a function of the initial target thickness  $L/\lambda_D$  is shown. In case of Maxwellian electrons—black dots and blue (dark gray) triangles represent numerical results of the nonrelativistic adiabatic and the kinetic Maxwellian approach, respectively—the final energy increases with increasing  $L/\lambda_D$  towards infinity. In contrast in the hydrodynamic approach, where red (gray) diamonds represent simulations for the nonrelativistic case with an adiabatic index  $\kappa = 3$ , the maximum ion energy saturates quickly with increasing  $L/\lambda_D$ . The green (light gray) curve depicts the analytical result for the maximum ion energy of the nonrelativistic adiabatic Maxwellian approach, given by Eq. (27). The dashed black line stands for the maximum ion energies from thick targets and nonrelativistic electrons with a steplike energy distribution ( $\kappa = 3$ ), as determined by Eq. (14). In (b) the total initial energy (per area) of the system as a function of the initial target thickness  $L/\lambda_D$  is plotted. The values were found in simulations with numerous foil thicknesses for the different models. Initially the total energy is contained in the electric field and the thermal energy of the electrons. The black dots correspond to Maxwell-like distributed electrons, while the red (gray) diamonds represent the hydrodynamic approach. For foil thicknesses  $L/\lambda_D \gtrsim 10$  the total initial energies in both models are approximately the same.

Therefore, the large discrepancy in the ion energies arises from the different temporal behavior of the electric field strength  $E(t)$  at the ion front, which is illustrated in Figs. 9(a) and 9(b). First, we notice that the fields in both models using Maxwellian electrons are almost identical over tens of ion plasma periods for thicker foils [Fig. 9(a)], whereas the adiabatic Maxwellian model predicts a faster decrease of the accelerating field in the case of thinner foils (see thick green line in Fig. 9(b) in comparison with the dashed black curve for the kinetic model). After  $\omega_{pi} t = 50$ , the field strengths will be reduced by approximately two orders of magnitude. In contrast, the hydrodynamic model predicts a much larger drop of the electric field—approximately four orders of magnitude during the same time interval.

In general, the electric field is given by  $E(t) = \sqrt{2/\epsilon_0} \sqrt{n_e(t)} T_e(t)$ . As Figs. 9(c) and 9(d) indicate, the temporal behavior of the electron density is similar for both types of models. Thus, the difference in the electric field strength at the ion front should be mainly influenced by the behavior of the electron temperature at that position. The graphs in Figs. 9(e) and 9(f) show the evolution of the electron temperature at the ion front. Obviously, the cooling process is much more pronounced in the hydrodynamic model.

To give a qualitative explanation for this behavior, we have to keep in mind that the adiabatic Maxwellian model uses a single, well-defined electron temperature, which is uniform in space, i.e.,  $T_e(x, t) = T_e(t)$ . The temporal variation of  $T_e(t)$  is caused by the transfer of thermal energy from electrons to kinetic energy of the ions via the electric field. At the

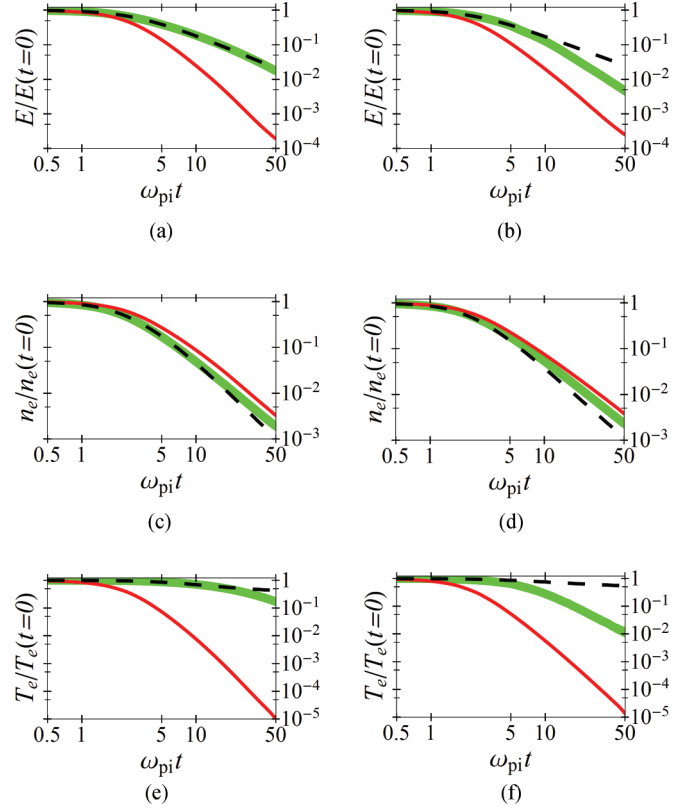


FIG. 9. (Color online) Simulation results of the electric field strength [panels (a) and (b)], the electron density [panels (c) and (d)], and the electron temperature [panels (e) and (f)] at the ion front as functions of time for targets with initial thicknesses  $L/\lambda_D = 80$  (left column) and  $L/\lambda_D = 2$  (right column), respectively. The curves are normalized to the corresponding initial values. The thick green (light gray) and dashed black curves follow from the nonrelativistic adiabatic and kinetic Maxwellian models, respectively. The results of the hydrodynamic ansatz are depicted by the solid (gray) red curves.

beginning of the expansion, the kinetic energy of the ions gained from the electric field is almost independent on the initial foil thickness, because the electric field at the ion boundary depends only weakly on  $L$  for  $L > \lambda_D$ . However, the total initial thermal energy of the electrons strongly depends on  $L$  (at constant  $n_{e,0}$  and  $T_{e,0}$ ), because the number of hot electrons increases proportionally with increasing target thickness.<sup>11</sup> Consequently, the relative energy loss of the hot electrons is smaller for thicker foils. Or, in other words, the temperature  $T_e(t)$  decreases more slowly. This argument also illustrates, why the adiabatic Maxwellian model converges into the isothermal model predicting an infinite maximum ion energy for  $L \rightarrow \infty$ .

Within the kinetic Maxwellian model, the temperature is not uniform in space as in the adiabatic Maxwellian approach.

<sup>11</sup>Note that from the experimental point of view, constant values of  $n_{e,0}$  and  $T_{e,0}$  with an increasing target thickness  $L$  imply a constant value of the laser intensity but an increasing focal spot radius and, therefore, an increasing pulse power. This follows from the discussion in Sec. V; see especially Eq. (38) for  $T_{e,0}$  and Eq. (36) for the electron plasma frequency (which can be resolved for  $n_{e,0}$ ).

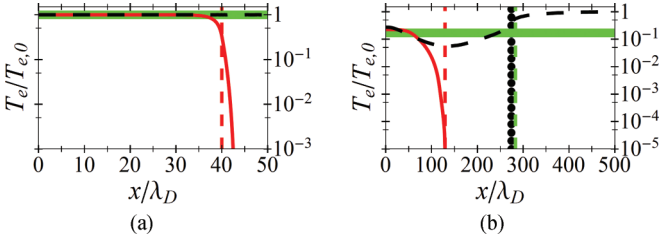


FIG. 10. (Color online) In panels (a) and (b), the simulation results for the spatial electron temperature distribution at two instants of time are plotted for  $\omega_{pi} t = 0$  and  $\omega_{pi} t = 50$ , respectively. The bold green (light gray) and black dashed curves correspond to Maxwellian electrons (adiabatic and kinetic ansatz, respectively), while the red (gray) curves show the results of the hydrodynamic approach ( $\kappa = 3$ ). The dashed red (gray) and green (light gray) vertical lines mark the ion fronts within the hydrodynamic and the adiabatic Maxwellian model, respectively, whereas the dotted black vertical line corresponds to the kinetic Maxwellian approach. Initially, the target thickness was  $L/\lambda_D = 80$  and the ion front was located at  $40 \lambda_D$ .

However, the deviation of the electron phase-space density  $f_{e,0}$  from the initial Maxwellian distribution is relatively small in the kinetic model during the essential acceleration time of the ions. Therefore, the evolution of the electric field strength as well as of the electron density and the electron temperature at the ion front are very similar to that of the adiabatic case during that period of time,  $\omega_{pi} t \lesssim 10$  (see Fig. 9).

In contrast, the hydrodynamic model gives a local temperature, which is connected to the spatial electron density distribution by the adiabatic relation  $T_e(x) = T_{e,0}(n_e(x)/n_{e,0})^{\kappa-1}$  (see Ref. [64]). As a consequence, the electron temperature drops rapidly at the ion front while the electron density is decreasing due to the expansion. The obtained effect is much stronger than the reduction of the electron temperature due to the total energy loss of all electrons in the adiabatic Maxwellian model. The differing properties of the spatial temperature profiles of the models are demonstrated in Fig. 10.

## V. DISCUSSION OF THE APPLICABILITY OF THE DIFFERENT MODELS FOR THE INTERPRETATION OF EXPERIMENTS

In this section we will compare the predictions of the plasma expansion models described above with the results of various experiments. Since PIC simulations commonly predict a Maxwellian electron distribution generated during the laser-plasma interaction, the observed ion acceleration is often described by the application of Mora's model [41] with a certain (empiric) acceleration time  $t_{acc}$  which is proportional to the laser pulse duration  $\tau_L$  (e.g., Refs. [9,70,71]). This procedure simply assumes that the laser keeps the electrons in a Maxwell distribution with a temperature approximately given by the ponderomotive potential [72]. Once the laser pulse is over, the hot electrons cool down, transferring a fraction of their energy to the ions, and the plasma expansion becomes adiabatic. The maximum ion energy is still increasing in this phase. Its final value will be reached in the limit  $t \rightarrow \infty$ , according to Ref. [57] and Eq. (25). However, this is a purely one-dimensional consideration.

In reality, the acceleration efficiency drops as soon as the plasma geometry becomes multidimensional. This happens approximately at the time when the displacement of the ion front in forward direction,  $x_{acc}$ , exceeds the transverse dimension  $D_e$  of the electron spot on the rear side of the target (e.g., Refs. [43,73,74]). The limitation of the acceleration distance decreases significantly the resulting ion energies (see Ref. [73]) in comparison to one-dimensional models used in Refs. [41,73]. Based on the results of Ref. [41], this time  $t_{1D \rightarrow 3D}$  can be estimated for protons as

$$\omega_{pi} t_{1D \rightarrow 3D} = (2 \exp(1))^{1/4} \sqrt{\frac{D_e}{\lambda_D}}, \quad (28)$$

which in physical units reads as

$$t_{1D \rightarrow 3D} \text{ (fs)} = 134.5 \sqrt{\frac{D_e \text{ (\mu m)}}{\sqrt{n_{e,0} \text{ (10}^{20} \text{ cm}^{-3})} T_{e,0} \text{ (MeV)}}}. \quad (29)$$

Following Ref. [9], the size of the electron spot on the rear target surface can approximately be evaluated with help of the relation  $D_e = D_L + 2 \tan(\theta_e) L$ . Here,  $D_L$  is the laser spot diameter on the target front side,  $L$  is the thickness of the target, and  $\theta_e$  is the half-opening angle of the electron beam inside the target. According to Ref. [9] one has  $\theta_e \approx 25^\circ$ . This value will be used throughout this section. Furthermore,  $D_L \approx 5 \mu\text{m} \dots 25 \mu\text{m}$  (e.g., Ref. [75] resp. Ref. [5]) and normally  $L \lesssim 100 \mu\text{m}$ . For the corresponding quantity  $D_e$  we get values within a range of approximately  $5 \mu\text{m} \dots 100 \mu\text{m}$ . Assuming hot electron temperatures in the range of  $T_{e,0} \approx 0.1 \text{ MeV} \dots 10 \text{ MeV}$  and densities  $n_{e,0} \approx 10^{20} \text{ cm}^{-3} \dots 10^{21} \text{ cm}^{-3}$ , we may calculate corresponding times  $t_{1D \rightarrow 3D}$  between 100 fs and 2500 fs.

For relatively long laser pulse durations,  $\tau_L \gtrsim 150$  fs, and assuming similar focusing conditions, the ion bunch already reaches a longitudinal extent of the order of the transverse size of the electron spot during the laser pulse duration. Therefore, the acceleration within the subsequent adiabatic regime is almost negligible and the relation  $t_{acc} \approx t_{1D \rightarrow 3D} \approx \tau_L$  holds. As a result, the isothermal theory (e.g., Refs. [9,41]) describes the acceleration process sufficiently well.

Although the maximum energy predicted by the isothermal model depends on several experimental quantities, a rough scaling with the laser intensity  $I_L$  times the square of the laser wavelength  $\lambda_L$  can be found,  $\varepsilon_{\max \text{ iso}} \propto \sqrt{I_L \lambda_L^2}$ , as it was given by Clark *et al.* in Ref. [76] and confirmed in Refs. [73,77]. We may derive this characteristic behavior by inserting relation (28) for the limited acceleration time into the expression for the maximum proton energy of Ref. [41],

$$\varepsilon_{\max \text{ iso}} = 2 T_{e,0} \operatorname{arcsinh}\left(\frac{\omega_{pi} t}{\sqrt{2 \exp(1)}}\right)^2. \quad (30)$$

In the linearized form we have

$$\varepsilon_{\max \text{ iso}} \approx \sqrt{\frac{2}{\exp(1)}} \frac{T_{e,0} D_e}{\lambda_D}. \quad (31)$$

Now, applying the estimates of Ref. [9] for the total number of hot electrons generated by the laser pulse,  $N_e = \eta \varepsilon_L / T_{e,0}$ , and for the hot electron density at the rear side of the target,  $n_e = 4 N_e / (\pi D_e^2 \tau_L c)$ , as well as the relation  $P_L = \varepsilon_L / \tau_L$ , with the

laser pulse power  $P_L$  and the laser pulse energy  $\varepsilon_L$  in the focal spot, respectively, one may rewrite the Debye length as

$$\lambda_D = \frac{D_e}{2} \sqrt{\frac{1}{\eta} \frac{\pi \varepsilon_0 c}{e^2} \frac{T_{e,0}^2}{P_L}}. \quad (32)$$

Here,  $\eta$  denotes the conversion efficiency of laser energy into hot electron energy within the laser focus. A typical value of the order of 10% (see, e.g., Ref. [74]) will be used in the estimates below.

From Eq. (32) we directly obtain the normalized electron spot size

$$\frac{D_e}{\lambda_D} = \sqrt{\eta} \frac{4 e^2}{\pi c \varepsilon_0} \frac{P_L}{T_{e,0}^2} \quad (33)$$

and substitute it into Eq. (31). We finally get

$$\begin{aligned} \varepsilon_{\max \text{ iso}} &\approx \sqrt{\eta} \sqrt{\frac{8}{\pi \exp(1)} \frac{e^2}{\varepsilon_0 c}} \sqrt{P_L} \\ &= \frac{r_L}{\lambda_L} \sqrt{\eta} \sqrt{\frac{8}{\exp(1)} \frac{e^2}{\varepsilon_0 c}} \sqrt{I_L \lambda_L^2} \end{aligned} \quad (34)$$

by relating the pulse power to the laser intensity,  $P_L = \pi r_L^2 I_L$ . In physical units we obtain

$$\varepsilon_{\max \text{ iso}} \text{ (MeV)} \approx 3.33 \frac{r_L}{\lambda_L} \sqrt{\eta} \sqrt{I_L \lambda_L^2 (10^{18} \text{ W cm}^{-2} \mu\text{m}^2)}. \quad (35)$$

Hence, we find  $\varepsilon_{\max \text{ iso}} \propto \sqrt{I_L \lambda_L^2}$ , in agreement with Refs. [76]. Note, again, that the scaling has been found by setting the acceleration distance  $x_{\text{acc}}$  equal to the transverse size of the electron spot on the rear side of the target. Moreover, by changing that acceleration distance to some multiple of the electron spot size,  $h D_e$ , the result (35) would simply become multiplied by this factor  $h$ . The same result would follow from an increase of the normalized focal radius by a factor of  $h$ ,  $h r_L/\lambda_L$ , while assuming the laser intensity  $I_L$  to remain constant. Therefore, the particular value of the acceleration distance  $x_{\text{acc}}$  does not influence the qualitative scaling law (35).

In the ultrashort-pulses regime  $\tau_L \lesssim 100$  fs the situation differs, because the acceleration time exceeds the laser pulse duration,  $t_{\text{acc}} \approx t_{1D \rightarrow 3D} > \tau_L$ . Hence, the adiabatic regime becomes important, and another scaling for the maximum ion energy should be obtained. This is demonstrated in Fig. 11, which is based on Fig. 7 of Ref. [78], where the results from a large number of laser-ion acceleration experiments from the past decades have been collected.

The difference between the two regimes, as shown in Fig. 11, was previously discussed also by Fuchs *et al.* [71]. Assuming isothermal Maxwellian electrons and laser pulse durations  $\tau_L \gtrsim 150$  fs, they found empirically a good agreement between experimental data and Eq. (30) by setting the acceleration time proportional to the laser pulse duration  $\tau_L$ . In contrast, they determined the acceleration time to be almost constant for ultrashort pulse durations,  $\tau_L < 60$  fs.

One can immediately show that a fixed acceleration time in Eq. (30) will result in a dependency of the maximum ion energy on  $T_{e,0}$  only—besides a factor, which contains the laser

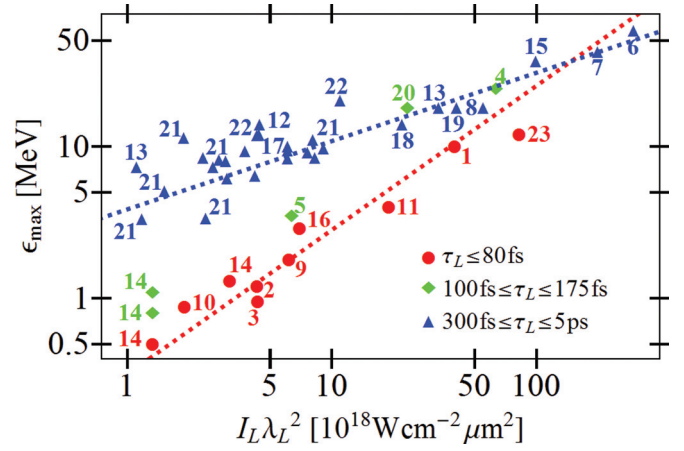


FIG. 11. (Color online) Overview of various experiments performed in the past decades. From the illustration it is obvious that ultrashort pulse experiments [red (gray) dots] show a different scaling than experiments with relatively long laser pulses [blue (dark gray) triangles]. Dotted lines with the corresponding color (grayscale values) are drawn in both regions to guide the eye. Experiments with intermediate pulse durations [green (light gray) diamonds] fall between both regions. The following experimental data have been used: 1 = [79], 2 = [80], 3 = [81], 4 = [82], 5 = [83], 6 = [5], 7 = [84], 8 = [7], 9 = [85], 10 = [86], 11 = [87], 12 = [88], 13 = [78], 14 = [70], 15 = [89], 16 = [74], 17 = [90], 18 = [91], 19 = [77], 20 = [92], 21 = [93], 22 = [94], 23 = [95].

wavelength, the conversion efficiency and the divergence of the electron beam as well as the ratio of the target thickness and the laser focal spot radius. For that we rewrite the ion plasma frequency in the form

$$\omega_{\text{pi}} = \frac{\sqrt{\eta}}{1 + \tan(\theta_e) \frac{L}{r_L}} \sqrt{\frac{Z_i e^2}{m_i \varepsilon_0 c} \frac{I_L}{T_{e,0}}}, \quad (36)$$

which in physical units assuming protons reads

$$\omega_{\text{pi}}(1/\text{fs}) = 0.019 \frac{\sqrt{\eta}}{1 + \tan(\theta_e) \frac{L}{r_L}} \sqrt{\frac{I_L (10^{18} \text{ W cm}^{-2})}{T_{e,0} \text{ (MeV)}}, \quad (37)$$

and express the laser intensity  $I_L$  in Eq. (36) in terms of  $T_{e,0}$  by using the relation

$$T_{e,0} = m_e c^2 \left( \sqrt{1 + \frac{I_L \lambda_L^2}{1.37 \times 10^{18} \text{ W cm}^{-2} \mu\text{m}^2}} - 1 \right) \quad (38)$$

of Wilks *et al.* [72]. By inserting the resulting expression into Eq. (30), we immediately confirm this statement. It is interesting to note that exactly the same conclusion for the maximum ion energy can be drawn assuming steplike distributed electrons, as shown in Eqs. (14) and (15), respectively. Moreover, the relation (14) fits the experimental results in the ultrashort pulse regime quite well (see Fig. 12).

To answer the question whether the illustrated agreement is only a consequence of the intrinsic adiabatic plasma description in the hydrodynamic model or if it is also related to the shape of the initial electron distribution, we checked the experimental data against the results of the Maxwellian adiabatic modeling (see Sec. III). According to the discussion

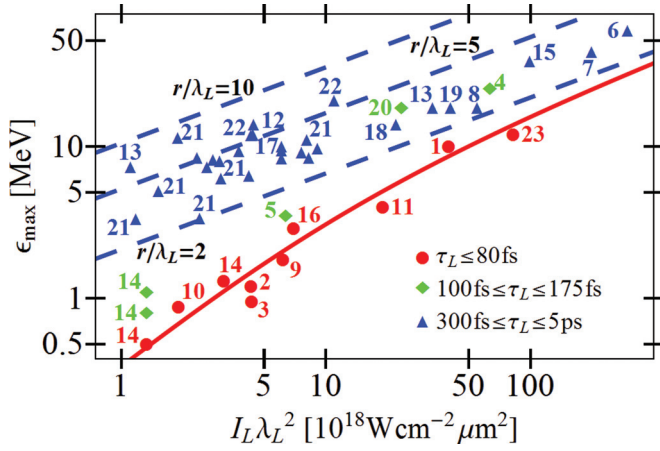


FIG. 12. (Color online) The  $\sqrt{I_L \lambda_L^2}$  scaling [blue (dark gray) dashed lines] according to Eq. (35) is shown for laser focal spot radii  $r_L = \{2, 5, 10\} \lambda_L$ . In addition, the red (gray) curve represents the maximum energy of the ions in the hydrodynamic ansatz applying Eq. (14). The experimental data are identical to those of Fig. 11.

of Sec. IV—see especially Fig. 8(a)—it is evident that the Maxwellian adiabatic expansion gives a different scaling. Figure 13 includes curves, which were calculated with help of relation (27) for three different normalized target thicknesses  $l = L/\lambda_D$  as well as the result from the hydrodynamic model.

In this context, we note that the applied relations (14) and (27) express the final energy of the ion front in the limit  $t, x \rightarrow \infty$ . In contrast, as discussed earlier in this section, the one-dimensional expansion—and, thus, the essential energy gain—occurs over a distance  $x_{\text{acc}}$  comparable to the transverse

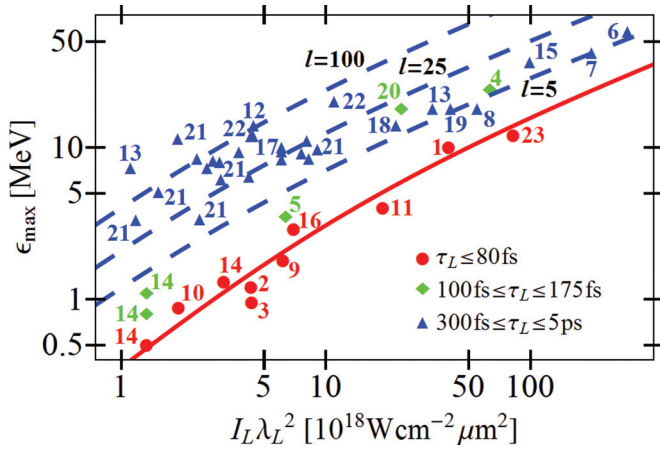


FIG. 13. (Color online) Comparison of the scaling of the different adiabatic models. While the red (gray) curve represents the maximum energy of the ions in the hydrodynamic ansatz calculated with Eq. (14), the blue (dark gray) dashed curves show the ion energies in case of Maxwellian electrons given by Eq. (27) for three normalized foil thicknesses  $l = L/\lambda_D = \{5, 25, 100\}$ . The experimental data are identical to those of Fig. 11. We remind that the plotted theoretical curves exhibit the maximum energies in the limit  $t \rightarrow \infty$ . Note also that an increase in the target thickness does not necessarily imply an increase of its normalized value for a given set of laser parameters ( $I_L, r_L, P_L, \dots$ ), since the Debye length (32) depends on the size of the electron spot on the rear side of the target, which itself changes with the target thickness.

size  $D_e$  of the electron sheath at the rear side of the target. Therefore, we have revisited the above comparison between the two models and the experimental data using a finite acceleration distance  $x_{\text{acc}}$ . We found out that this limitation in the acceleration process does not change the general scaling remarkably. Instead the two models still predict two clearly different scaling laws. In any case, the adiabatic Maxwellian model cannot reproduce the scaling implied by the ultrashort pulse experiments over the complete intensity region ( $10^{18} \text{ W cm}^{-2}$ – $10^{20} \text{ W cm}^{-2}$ ). In contrast, the experimental data for the maximum ion energy in the ultrashort pulse regime may be interpreted well by the hydrodynamic approach.

Since the most important difference between both models is the non-Maxwellian electron distribution in the hydrodynamic approach, this could be an indication for the presence of non-Maxwellian electron spectra generated in ultrashort pulse interactions. This suggestion is supported by the statement in Ref. [43] whereby about 100 fs are needed to evolve the hot electrons into an equilibrium distribution, as well as by simulations in Ref. [96], where a non-Maxwellian distribution has been observed using an ultrashort pulse laser ( $\tau_L = 60$  fs). Also we note here about the interaction schemes with truncated Maxwellian distributions discussed in Refs. [46–51]. This type of energy distribution functions may be induced by the escape of the fastest electrons from the charge separation region. A plausible explanation for this possibility follows from the multidimensional nature of the interaction, which does not provide an equilibrium solution for Maxwellian electrons [97]. Because of a finite potential at infinity in this geometry, electrons with kinetic energies exceeding this potential, can escape from the target and a non-Maxwellian distribution will be formed.

As a non-Maxwellian electron distribution should also manifest itself in the shape of the proton spectrum, we checked that issue in the publications employed in the Figs. 11–13 and compared it with the theoretical prediction of the hydrodynamic model, Eq. (17), as well as with the theoretical spectrum evaluated for Maxwellian electrons [41],

$$\frac{\partial^2 N}{\partial \varepsilon \partial A} = \frac{n_{i,0} c_s t}{\sqrt{2 Z_i T_{e,0}} \varepsilon} \exp\left(-\sqrt{\frac{2 \varepsilon}{Z_i T_{e,0}}}\right). \quad (39)$$

As mentioned in Sec. II, the hydrodynamic result (17) becomes identical with Eq. (39) in the limit  $\kappa \rightarrow 1$ , where the electron spectrum associated with the hydrodynamic ansatz takes the form of a Maxwellian distribution (see Ref. [61]). To compare the experimental data with the theoretical models, we have fitted the expressions (17) and (39) to the measured data. In the case of the hydrodynamic model, the adiabatic index  $\kappa$  was used as a fit parameter. The deviation of its best-fit value  $\kappa_{\text{fit}}$  from unity may be considered as a measure for the deviation of the electron energy distribution from a Maxwellian one.

In our analysis we noticed that  $\kappa_{\text{fit}}$  is close to 1 for a large number of experiments using relatively long laser pulse durations,  $\tau_L \geq 300$  fs. Hence, the corresponding proton spectra are quite well described by the theoretical result (39) assuming Maxwellian electrons. This is obvious from the right column of panels in Fig. 14, where the best-fit results for the hydrodynamic expression (green solid lines) are almost identical with the best-fit results for the Maxwellian case (red dashed lines). In contrast, for numerous ultrashort pulse

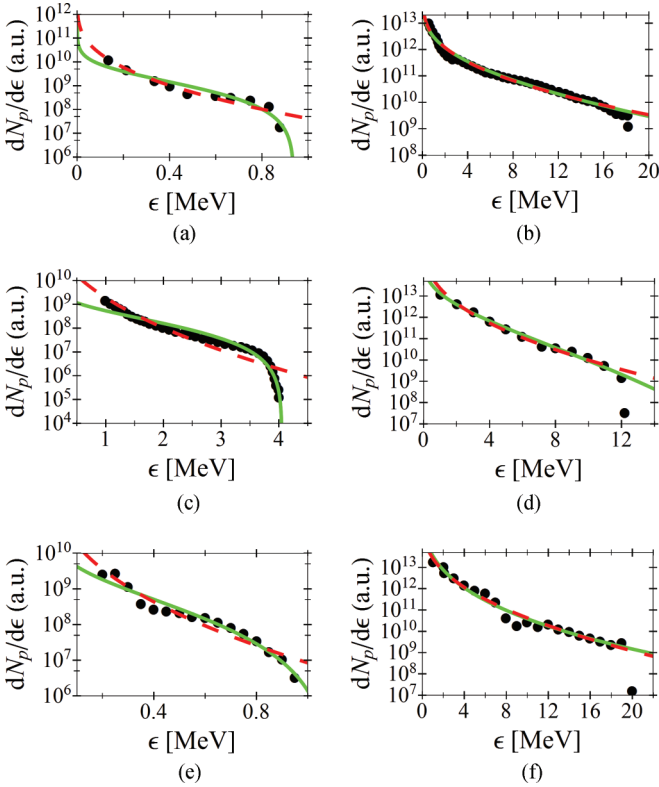


FIG. 14. (Color online) The plot shows the experimental data (black dots) for the proton spectrum from some of the references used in the Figs. 11–13. While the left column of panels corresponds to ultrashort pulse experiments ( $\tau_L \leq 80$  fs), the right one concerns experiments with relatively long laser pulse durations ( $\tau_L \geq 300$  fs). The best fit for the theoretical ion spectrum under the assumption of Maxwellian electrons (39) is depicted by red (gray) dashed lines. The corresponding fit of the hydrodynamic result (17) shows up as a green (light gray) solid curve. Thereby, the adiabatic constant  $\kappa$  is considered as a fit parameter and its best-fit value is given by  $\kappa_{\text{fit}}$ . This number is close to 1 in case of the experiments using relatively long laser pulse durations, while it is close to values 2–3 for the ultra short pulse experiments. The following data and characteristics correspond to the different panels: (a) data from Ref. [86],  $\tau_L = 70$  fs,  $I_L = 3 \times 10^{18}$  W cm $^{-2}$ ,  $\varepsilon_{\text{max}} = 0.88$  MeV,  $\kappa_{\text{fit}} = 2.32$ , (b) data from Ref. [78],  $\tau_L = 350$  fs,  $I_L = 3 \times 10^{19}$  W cm $^{-2}$ ,  $\varepsilon_{\text{max}} = 18$  MeV,  $\kappa_{\text{fit}} = 1.08$ , (c) data from Ref. [87],  $\tau_L = 34$  fs,  $I_L = 3 \times 10^{19}$  W cm $^{-2}$ ,  $\varepsilon_{\text{max}} = 4$  MeV,  $\kappa_{\text{fit}} = 2.19$ , (d) data from Ref. [94],  $\tau_L = 600$  fs,  $I_L = 4 \times 10^{18}$  W cm $^{-2}$ ,  $\varepsilon_{\text{max}} = 12$  MeV,  $\kappa_{\text{fit}} = 1.24$ , (e) data from Ref. [81],  $\tau_L = 60$  fs,  $I_L = 7 \times 10^{18}$  W cm $^{-2}$ ,  $\varepsilon_{\text{max}} = 0.95$  MeV,  $\kappa_{\text{fit}} = 1.79$ , and (f) data from Ref. [94],  $\tau_L = 700$  fs,  $I_L = 1 \times 10^{19}$  W cm $^{-2}$ ,  $\varepsilon_{\text{max}} = 20$  MeV,  $\kappa_{\text{fit}} = 0.93$ .

experiments ( $\tau_L \leq 80$  fs) the best-fit values for  $\kappa$  are close to numbers<sup>12</sup> 2–3, as illustrated in the left column of Fig. 14. However, we want to emphasize that this is not necessarily a direct proof for the presence of a steplike electron energy distribution in those ultrashort pulse experiments, since the

<sup>12</sup>Here we want to remind that values of 2 and 3 for  $\kappa$  are associated with a steplike distribution function in the ultrarelativistic and the nonrelativistic limit, respectively (see Ref. [61]).

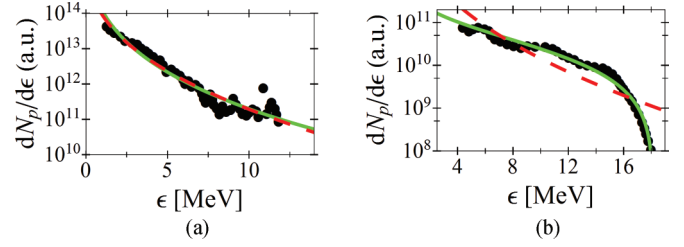


FIG. 15. (Color online) Illustration of two exceptional cases for the proton spectrum as compared to the default case which is illustrated in Fig. 14. Here, the best-fit for the hydrodynamic expression (17) is almost identical to the Maxwellian result (39) in the case of the ultrashort pulse experiment shown in (a), while this is not the case for the experiment using a relatively long pulse duration depicted in (b). The following data and characteristics correspond to the different panels: (a) data from Ref. [95]:  $\tau_L = 50$  fs,  $I_L = 1.3 \times 10^{20}$  W cm $^{-2}$ ,  $\varepsilon_{\text{max}} = 12$  MeV,  $\kappa_{\text{fit}} = 0.88$  and (b) data from Ref. [77]:  $\tau_L = 300$  fs,  $I_L = 3.7 \times 10^{19}$  W cm $^{-2}$ ,  $\varepsilon_{\text{max}} = 18$  MeV,  $\kappa_{\text{fit}} = 2.46$ .

shape of the proton spectra are in reality influenced by various other aspects, such as the laser prepulse and multidimensional as well as multi-ion species effects. But the results reported above support the suggestion about the presence of a non-Maxwellian distribution in those experiments.

As demonstrated in Fig. 15, we found also some exceptional cases in the analysis of the diagnosed proton spectra. Nevertheless, we believe that there is some evidence for a non-Maxwellian distribution in most of the analyzed ultrashort pulse experiments as well as for a Maxwellian electron spectrum in the regime with relatively long laser pulse durations. Of course, in reality the details of the laser pulse as well as of the target parameters are likely to have a noticeable influence on the shape of the electron distribution, too.

We also want to point out that—beside the shape of the electron energy distribution—there could also be other explanations for the discrepancy between the results of the plasma expansion model using a Maxwellian hot electron energy distribution and the experimental results at ultrashort laser pulses. A different scaling of the electron temperature as a function of the laser intensity in the ultrashort pulse regime might be a first reason (see Fig. 16). A deviation of the electron temperature from the broadly used pondermotive scaling law (38) was supposed in Ref. [98] and observed numerically for ultrashort laser pulses in Ref. [99]. In a more general sense, the assumption of a stationary electron distribution—which is essential for the basic model (1)—may not be fulfilled in the ultrashort pulse regime. To overcome these uncertainties, further investigations of the hot electron spectra—experimentally as well as theoretically—are necessary.

Furthermore, we want to note that the comparison of the results from numerous experiments, which were carried out on different laser systems, in respect to the parameter  $I_L \lambda_L^2$  (as shown in Fig. 14) may be oversimplifying. It is clear that—in addition to the quantity  $I_L \lambda_L^2 \sim a_0^2$ —numerous other parameters and their complex interplay are likely to influence the interaction and, hence, the maximum ion energy. It has been shown that parameters such as the laser pulse duration [100], the focal spot size and the laser power [101], the temporal shape of the laser beam and its prepulse intensity [83], the

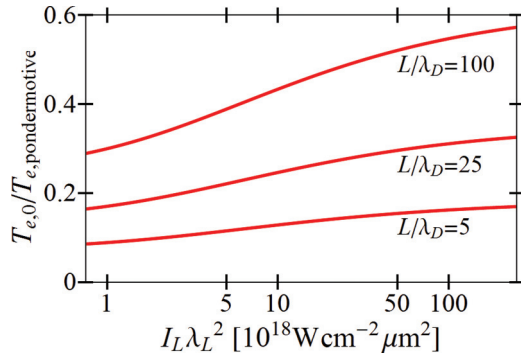


FIG. 16. (Color online) The laser intensity scaling of the electron temperature in relation to the ponderomotive approximation (38) under the condition of equal maximum ion energies from the adiabatic plasma expansion with Maxwellian hot electrons, given by Eq. (27), and from the hydrodynamic ansatz following Eq. (14). Thereby, the result is shown for three values of the normalized target thickness  $L/\lambda_D$ .

target thickness [9,83], etc., may have an impact on the ion acceleration process.

Also, we note that our discussion of experimental findings and the related intensity scaling of maximum ion energies refers to laser pulse intensities below  $10^{20} \text{ W cm}^{-2}$ . Recently performed experiments at higher laser intensities [102] demonstrate a different intensity scaling, if we compare the observed maximum ion energies with the scaling law for the ultrashort pulse experiments collected in Fig. 11 after its extrapolation to higher intensity values. Moreover, the absolute numbers of the maximum ion energy observed in Ref. [102] are lower by almost one order of magnitude in comparison with the numbers predicted by the scaling relation (15) applied to intensities above  $10^{20} \text{ W cm}^{-2}$ . The established disagreement might be caused by different characteristics of the electron heating process at these high laser intensities, for example. Further efforts are needed to understand this in detail.

## VI. SUMMARY

Starting from a hydrodynamic approach, which implies a steplike energy distribution for the hot electrons, we calculated a self-similar solution for the adiabatically expanding plasma. It includes the well-known self-similar solution [1,2,39] for the expansion under isothermal Maxwellian electrons as a limiting case. Moreover, we were able to formulate empirical expressions for the electric field strength, velocity and position of the ion front. In analogy, we extended the study of Mora [57] describing the adiabatic expansion of a plasma driven by hot Maxwellian electrons.

Comparing the results of the different models, we have found that the hydrodynamic approach leads to a remark-

ably different evolution of the ion acceleration process in comparison with the models using Maxwellian distributions, even though approximately the same initial parameters such as temperature, density, and total thermal energy for the hot electrons were assumed. Thereby it turned out that the different shape of the hot electron energy distribution in the hydrodynamical approach leads to a rapidly dropping electron temperature at the ion front in contrast to the Maxwellian models, which gives rise to much lower maximum ion energies.

Furthermore, we have compared our analytical estimates to experimental results looking at the maximum kinetic energy and the spectrum of the accelerated protons and ions. Here, we obtained a surprisingly good agreement between results for the maximum ion energy of the hydrodynamic model, implying a steplike hot electron energy distribution, and the data from experiments with laser pulse durations shorter than 80 fs. These model predictions fit to the measured ion energies in absolute numbers as well as in matters of the intensity scaling. In contrast, the plasma expansion models which are based on a Maxwellian hot electron energy distribution do not reproduce the experimentally observed intensity scaling.

Moreover, besides some exceptional examples, in the majority of the investigated experiments, the measured spectra are more likely described by the theoretical ion spectrum linked to hydrodynamic approach rather than by the ion spectrum associated with Maxwellian electrons. Based on that insights we may suspect that non-Maxwellian electron energy distributions are often involved in this kind of experiment.

One reason for the presence of non-Maxwellian electron energy distributions in ultrashort pulse experiments might be that during the generation of the hot-electron population by the laser the pulse duration is too short to allow for the formation of a distinct Maxwellian distribution of the electrons. Therefore, we believe that the different shape of the electron phase-space density gives rises to the observed discrepancy. Hence, we reason that it is necessary to pay more attention to the particular electron distribution function in future theoretical studies and in experiments. This includes the investigation of the Maxwellian character of the energy distribution itself, e.g., in dependence on the pulse length of the driving laser beam. It comprises also the knowledge of the scaling laws for the hot electron temperature in case of an obtainable equilibrium distribution function.

## ACKNOWLEDGMENTS

The authors thank A. A. Andreev (Max-Born Institute for Optics, Berlin) for valuable discussions, which have strongly motivated this work. The research leading to these results has received partial funding from the BMBF (03ZIK445 and 03Z1H531) and from the DFG (TR18).

- [1] M. Widner, I. Alexeff, and W. D. Jones, *Phys. Fluids* **14**, 795 (1971).
- [2] J. E. Crow, P. L. Auer, and J. E. Allen, *J. Plasma Phys.* **14**, 65 (1975).
- [3] L. M. Wickens, J. E. Allen, and P. T. Rumsby, *Phys. Rev. Lett.* **41**, 243 (1978).

- [4] J. Denavit, *Phys. Fluids* **22**, 1384 (1979).
- [5] R. A. Snavely, M. H. Key, S. P. Hatchett, T. E. Cowan, M. Roth, T. W. Phillips, M. A. Stoyer, E. A. Henry, T. C. Sangster, M. S. Singh, S. C. Wilks, A. MacKinnon, A. Offenberger, D. M. Pennington, K. Yasuike, A. B. Langdon, B. F. Lasinski, J. Johnson, M. D.

- Perry, and E. M. Campbell, *Phys. Rev. Lett.* **85**, 2945 (2000).
- [6] S. P. Hatchett, C. G. Brown, T. E. Cowan, E. A. Henry, J. S. Johnson, M. H. Key, J. A. Koch, A. B. Langdon, B. F. Lasinski, R. W. Lee, A. J. Mackinnon, D. M. Pennington, M. D. Perry, T. W. Phillips, M. Roth, T. C. Sangster, M. S. Singh, R. A. Snavely, M. A. Stoyer, S. C. Wilks, and K. Yasuike, *Phys. Plasmas* **7**, 2076 (2000).
- [7] E. L. Clark, K. Krushelnick, J. R. Davies, M. Zepf, M. Tatarakis, F. N. Beg, A. Machacek, P. A. Norreys, M. I. K. Santala, I. Watts, and A. E. Dangor, *Phys. Rev. Lett.* **84**, 670 (2000).
- [8] S. C. Wilks, A. B. Langdon, T. E. Cowan, M. Roth, M. Singh, S. Hatchett, M. H. Key, D. Pennington, A. MacKinnon, and R. A. Snavely, *Phys. Plasmas* **8**, 542 (2001).
- [9] J. Fuchs, P. Antici, E. D'Humières, E. Lefebvre, M. Borghesi, E. Brambrink, C. A. Cecchetti, M. Kaluza, V. Malka, M. Manclossi, S. Meyroneinc, P. Mora, J. Schreiber, T. Toncian, H. Pépin, and P. Audebert, *Nat. Phys.* **2**, 48 (2006).
- [10] J. Fuchs, T. E. Cowan, P. Audebert, H. Ruhl, L. Gremillet, A. Kemp, M. Allen, A. Blazevic, J.-C. Gauthier, M. Geissel, M. Hegelich, S. Karsch, P. Parks, M. Roth, Y. Sentoku, R. Stephens, and E. M. Campbell, *Phys. Rev. Lett.* **91**, 255002 (2003).
- [11] T. E. Cowan, J. Fuchs, H. Ruhl, A. Kemp, P. Audebert, M. Roth, R. Stephens, I. Barton, A. Blazevic, E. Brambrink, J. Cobble, J. Fernández, J.-C. Gauthier, M. Geissel, M. Hegelich, J. Kaae, S. Karsch, G. P. Le Sage, S. Letzring, M. Manclossi, S. Meyroneinc, A. Newkirk, H. Pépin, and N. Renard-LeGalloudec, *Phys. Rev. Lett.* **92**, 204801 (2004).
- [12] M. Borghesi, A. J. Mackinnon, D. H. Campbell, D. G. Hicks, S. Kar, P. K. Patel, D. Price, L. Romagnani, A. Schiavi, and O. Willi, *Phys. Rev. Lett.* **92**, 055003 (2004).
- [13] M. Passoni, V. T. Tikhonchuk, M. Lontano, and V. Y. Bychenkov, *Phys. Rev. E* **69**, 026411 (2004).
- [14] S. V. Bulanov, T. Z. Esirkepov, V. S. Khoroshkov, A. V. Kuznetsov, and F. Pegoraro, *Phys. Lett. A* **299**, 240 (2002).
- [15] E. Fourkal, B. Shahine, M. Ding, J. S. Li, T. Tajima, and C. M. Ma, *Med. Phys.* **29**, 2788 (2002).
- [16] C. M. Ma, E. Fourkal, I. Veltchev, J. S. Li, J. Fan, T. Lin, and A. Tafo, in *World Congress on Medical Physics and Biomedical Engineering, September 7–12, 2009, Munich, Germany* (Springer, Berlin, 2010), pp. 66–69.
- [17] M. Borghesi, A. Schiavi, D. H. Campbell, M. G. Haines, O. Willi, A. J. MacKinnon, L. A. Gizzi, M. Galimberti, R. J. Clarke, and H. Ruhl, *Plasma Phys. Controlled Fusion* **43**, A267 (2001).
- [18] J. A. Cobble, R. P. Johnson, T. E. Cowan, N. Renard-Le Galloudec, and M. Allen, *J. Appl. Phys.* **92**, 1775 (2002).
- [19] C. A. Cecchetti, M. Borghesi, J. Fuchs, G. Schurtz, S. Kar, A. Macchi, L. Romagnani, P. A. Wilson, P. Antici, R. Jung, J. Osterholtz, C. A. Pipahl, O. Willi, A. Schiavi, M. Notley, and D. Neely, *Phys. Plasmas* **16**, 043102 (2009).
- [20] L. Willingale, P. M. Nilson, M. C. Kaluza, A. E. Dangor, R. G. Evans, P. Fernandes, M. G. Haines, C. Kamperidis, R. J. Kingham, C. P. Ridgers, M. Sherlock, A. G. R. Thomas, M. S. Wei, Z. Najmudin, K. Krushelnick, S. Bandyopadhyay, M. Notley, S. Minardi, M. Tatarakis, and W. Rozmus, *Phys. Plasmas* **17**, 043104 (2010).
- [21] P. K. Patel, A. J. Mackinnon, M. H. Key, T. E. Cowan, M. E. Foord, M. Allen, D. F. Price, H. Ruhl, P. T. Springer, and R. Stephens, *Phys. Rev. Lett.* **91**, 125004 (2003).
- [22] N. C. Woolsey, C. D. Gregory, R. Kodama, M. Koenig, B. Loupias, S. A. Myers, A. Oya, and Y. Sakawa, in *Journal of Physics: Conference Series*, Vol. 112 (IOP Publishing, Bristol, UK, 2008), p. 042009.
- [23] H.-S. Park, D. D. Ryutov, J. S. Ross, N. L. Kugland, S. H. Glenzer, C. Plechaty, S. M. Pollaine, B. A. Remington, A. Spitkovsky, L. Gargate, G. Gregori, A. Bell, C. Murphy, Y. Sakawa, Y. Kuramitsu, T. Morita, H. Takabe, D. H. Froula, G. Fiksel, F. Miniati, M. Koenig, A. Ravasio, A. Pelka, E. Liang, N. Woolsey, C. C. Kuranz, R. P. Drake, and M. J. Grosskopf, *High Energy Density Phys.* **8**, 38 (2012).
- [24] T. Z. Esirkepov and S. V. Bulanov, arXiv:1202.4552 (2012).
- [25] K. W. D. Ledingham, P. McKenna, and R. P. Singhal, *Science* **300**, 1107 (2003).
- [26] S. Kimura and A. Bonasera, *Nucl. Instrum. Methods A* **637**, 164 (2011).
- [27] K. Krushelnick, E. L. Clark, R. Allott, F. N. Beg, C. N. Danson, A. Machacek, V. Malka, Z. Najmudin, D. Neely, P. A. Norreys, M. R. Salvati, M. I. K. Santala, M. Tatarakis, I. Watts, M. Zepf, and A. E. Dangor, *IEEE Trans. Plasma Sci.* **28**, 1110 (2000).
- [28] R. Kodama, P. A. Norreys, K. Mima, A. E. Dangor, R. G. Evans, H. Fujita, Y. Kitagawa, K. Krushelnick, T. Miyakoshi, N. Miyanaga, T. Norimatsu, S. J. Rose, T. Shozaki, K. Shigemori, A. Sunahara, M. Tampo, K. A. Tanaka, Y. Toyama, T. Yamanaka, and M. Zepf, *Nature* **412**, 798 (2001).
- [29] M. Roth, T. E. Cowan, M. H. Key, S. P. Hatchett, C. Brown, W. Fountain, J. Johnson, D. M. Pennington, R. A. Snavely, S. C. Wilks, K. Yasuike, H. Ruhl, P. Pegoraro, S. V. Bulanov, E. M. Campbell, M. D. Perry, and H. Powell, *Phys. Rev. Lett.* **86**, 436 (2001).
- [30] H. Hora, J. Badziak, M. N. Read, Y.-T. Li, T.-J. Liang, Y. Cang, H. Liu, Z.-M. Sheng, J. Zhang, F. Osman, G. H. Miley, W. Zhang, X. He, H. Peng, S. Glowacz, S. Jablonski, J. Wolowski, Z. Skladanowski, K. Jungwirth, K. Rohlena, and J. Ullschmied, *Phys. Plasmas* **14**, 072701 (2007).
- [31] N. Naumova, T. Schlegel, V. T. Tikhonchuk, C. Labaune, I. V. Sokolov, and G. Mourou, *Phys. Rev. Lett.* **102**, 025002 (2009).
- [32] J. C. Fernandez, B. J. Albright, K. J. Bowers, D. C. Gautier, B. M. Hegelich, C.-K. Huang, D. Jung, S. Letzring, S. Palaniyappan, R. Shah, L. Yin, H.-C. Wu, and J. J. Honrubia, in *APS Meeting Abstracts* (American Society of Physics, Washington, DC, 2011), p. 7003.
- [33] V. Tikhonchuk, T. Schlegel, C. Regan, M. Temporal, J.-L. Feugeas, P. Nicolai, and X. Ribeyre, *Nucl. Fusion* **50**, 045003 (2010).
- [34] C. Regan, T. Schlegel, V. T. Tikhonchuk, J. J. Honrubia, J.-L. Feugeas, and P. Nicolai, *Plasma Phys. Controlled Fusion* **53**, 045014 (2011).
- [35] A. Modena, Z. Najmudin, A. E. Dangor, C. E. Clayton, K. A. Marsh, C. Joshi, V. Malka, C. B. Darrow, C. Danson, D. Neely, and F. N. Walsh, *Nature* **377**, 606 (1995).
- [36] V. Malka, S. Fritzler, E. Lefebvre, M.-M. Aleonard, F. Burgy, J.-P. Chambaret, J.-F. Chemin, K. Krushelnick, G. Malka, S. P. D. Mangles, Z. Najmudin, M. Pittman, J.-P. Rousseau, J.-N. Scheurer, B. Walton, and A. E. Dangor, *Science* **298**, 1596 (2002).

- [37] L. Gremillet, G. Bonnaud, and F. Amiranoff, *Phys. Plasmas* **9**, 941 (2002).
- [38] M. Tatarakis, F. N. Beg, E. L. Clark, A. E. Dangor, R. D. Edwards, R. G. Evans, T. J. Goldsack, K. W. D. Ledingham, P. A. Norreys, M. A. Sinclair, M.-S. Wei, M. Zepf, and K. Krushelnick, *Phys. Rev. Lett.* **90**, 175001 (2003).
- [39] A. V. Gurevich, L. V. Pariiskaya, and L. P. Pitaevskii, *Sov. Phys. JETP* **22**, 449 (1966).
- [40] J. E. Allen and J. G. Andrews, *J. Plasma Phys.* **4**, 187 (1970).
- [41] P. Mora, *Phys. Rev. Lett.* **90**, 185002 (2003).
- [42] V. T. Tikhonchuk, A. A. Andreev, S. G. Bochkarev, and V. Y. Bychenkov, *Plasma Phys. Contr. F.* **47**, B869 (2005).
- [43] S. G. Bochkarev, V. Y. Bychenkov, and V. T. Tikhonchuk, *Plasma Phys. Rep.* **32**, 205 (2006).
- [44] D. Cubero, J. Casado-Pascual, J. Dunkel, P. Talkner, and P. Hänggi, *Phys. Rev. Lett.* **99**, 170601 (2007).
- [45] C. Thauray, P. Mora, J. C. Adam, and A. Héron, *Phys. Plasmas* **16**, 093104 (2009).
- [46] J. S. Pearlman and R. L. Morse, *Phys. Rev. Lett.* **40**, 1652 (1978).
- [47] Y. Kishimoto, K. Mima, T. Watanabe, and K. Nishikawa, *Phys. Fluids* **26**, 2308 (1983).
- [48] M. Lontano and M. Passoni, *Phys. Plasmas* **13**, 042102 (2006).
- [49] M. Passoni and M. Lontano, *Phys. Rev. Lett.* **101**, 115001 (2008).
- [50] K. Quinn, P. A. Wilson, C. A. Cecchetti, B. Ramakrishna, L. Romagnani, G. Sarri, L. Lancia, J. Fuchs, A. Pipahl, T. Toncian, O. Willi, R. J. Clarke, D. Neely, M. Notley, P. Gallegos, D. C. Carroll, M. N. Quinn, X. H. Yuan, P. McKenna, T. V. Liseykina, A. Macchi, and M. Borghesi, *Phys. Rev. Lett.* **102**, 194801 (2009).
- [51] M. Passoni, L. Bertagna, and A. Zani, *New J. Phys.* **12**, 045012 (2010).
- [52] V. F. Kovalev, V. Y. Bychenkov, and V. T. Tikhonchuk, *J. Exp. Theor. Phys. Lett.* **74**, 10 (2001).
- [53] V. F. Kovalev, V. Y. Bychenkov, and V. T. Tikhonchuk, *J. Exp. Theor. Phys.* **95**, 226 (2002).
- [54] D. Bennaceur-Doumaz and M. Djebli, *Phys. Plasmas* **17**, 074501 (2010).
- [55] B. N. Breizman and A. V. Arefiev, *Phys. Plasmas* **14**, 073105 (2007).
- [56] B. Bezzerides, D. W. Forslund, and E. L. Lindman, *Phys. Fluids* **21**, 2179 (1978).
- [57] P. Mora, *Phys. Rev. E* **72**, 056401 (2005).
- [58] A. V. Brantov, V. T. Tikhonchuk, V. Y. Bychenkov, and S. G. Bochkarev, *Phys. Plasmas* **16**, 043107 (2009).
- [59] A. Diaw and P. Mora, *Phys. Rev. E* **84**, 036402 (2011).
- [60] A. Diaw and P. Mora, *Phys. Rev. E* **86**, 026403 (2012).
- [61] T. Kiefer and T. Schlegel, *Phys. Plasmas* **19**, 102101 (2012).
- [62] C. Sack and H. Schamel, *Phys. Rep.* **156**, 311 (1987).
- [63] A. Andreev, A. Lévy, T. Ceccotti, C. Thauray, K. Y. Platonov, R. A. Loch, and P. Martin, *Phys. Rev. Lett.* **101**, 155002 (2008).
- [64] A. A. Andreev, S. Steinke, T. Sokollik, M. Schnürer, S. Ter-Avetisyan, K. Y. Platonov, and P. V. Nickles, *Phys. Plasmas* **16**, 013103 (2009).
- [65] P. Mora and R. Pellat, *Phys. Fluids* **22**, 2300 (1979).
- [66] T. Grismayer and P. Mora, *Phys. Plasmas* **13**, 032103 (2006).
- [67] T. Grismayer, P. Mora, J. C. Adam, and A. Héron, *Phys. Rev. E* **77**, 066407 (2008).
- [68] P. Mora and T. Grismayer, *Phys. Rev. Lett.* **102**, 145001 (2009).
- [69] V. Y. Bychenkov, N. V. Novikov, D. Batani, V. T. Tikhonchuk, and S. G. Bochkarev, *Phys. Plasmas* **11**, 3242 (2004).
- [70] Y. Oishi, T. Nayuki, T. Fujii, Y. Takizawa, X. Wang, T. Yamazaki, K. Nemoto, T. Kayoiji, T. Sekiya, K. Horioka, Y. Okano, Y. Hironaka, K. G. Nakamura, K. Kondo, and A. A. Andreev, *Phys. Plasmas* **12**, 073102 (2005).
- [71] J. Fuchs, Y. Sentoku, E. D’Humières, T. E. Cowan, J. Cobble, P. Audebert, A. Kemp, A. Nikroo, P. Antici, E. Brambrink, A. Blazevic, E. M. Campbell, J. C. Fernández, J.-C. Gauthier, M. Geissel, M. Hegelich, S. Karsch, H. Popescu, N. Renard-Legalloudec, M. Roth, J. Schreiber, R. Stephens, and H. Pépin, *Phys. Plasmas* **14**, 053105 (2007).
- [72] S. C. Wilks, W. L. Kruer, M. Tabak, and A. B. Langdon, *Phys. Rev. Lett.* **69**, 1383 (1992).
- [73] L. Robson, P. T. Simpson, R. J. Clarke, K. W. D. Ledingham, F. Lindau, O. Lundh, T. McCanny, P. Mora, D. Neely, C.-G. Wahlström, M. Zepf, and P. McKenna, *Nat. Phys.* **3**, 58 (2007).
- [74] O. Jäckel, J. Polz, S. M. Pfotenhauer, H. P. Schlenvoigt, H. Schwoerer, and M. C. Kaluza, *New J. Phys.* **12**, 103027 (2010).
- [75] M. C. Kaluza, Ph.D. thesis, Max-Planck-Institut für Quantenoptik Garching (2004).
- [76] E. L. Clark, K. Krushelnick, M. Zepf, F. N. Beg, M. Tatarakis, A. Machacek, M. I. K. Santala, I. Watts, P. A. Norreys, and A. E. Dangor, *Phys. Rev. Lett.* **85**, 1654 (2000).
- [77] M. Allen, Y. Sentoku, P. Audebert, A. Blazevic, T. Cowan, J. Fuchs, J. C. Gauthier, M. Geissel, M. Hegelich, S. Karsch, E. Morse, P. K. Patel, and M. Roth, *Phys. Plasmas* **10**, 3283 (2003).
- [78] J. Fuchs, P. Audebert, M. Borghesi, H. Pépin, and O. Willi, *C. R. Phys.* **10**, 176 (2009).
- [79] V. Malka, S. Fritzler, E. Lefebvre, E. d’Humières, R. Ferland, G. Grillon, C. Albaret, S. Meyroneinc, J.-P. Chambaret, A. Antonetti, and D. Hulin, *Med. Phys.* **31**, 1587 (2004).
- [80] T. Fujii, Y. Oishi, T. Nayuki, Y. Takizawa, K. Nemoto, T. Kayoiji, K. Horioka, Y. Okano, Y. Hironaka, K. G. Nakamura, and K.-I. Kondo, *Appl. Phys. Lett.* **83**, 1524 (2003).
- [81] I. Spencer, K. W. D. Ledingham, P. McKenna, T. McCanny, R. P. Singhal, P. S. Foster, D. Neely, A. J. Langley, E. J. Divall, C. J. Hooker, R. J. Clarke, P. A. Norreys, E. L. Clark, K. Krushelnick, and J. R. Davies, *Phys. Rev. E* **67**, 046402 (2003).
- [82] A. J. Mackinnon, Y. Sentoku, P. K. Patel, D. W. Price, S. Hatchett, M. H. Key, C. Andersen, R. Snavely, and R. R. Freeman, *Phys. Rev. Lett.* **88**, 215006 (2002).
- [83] M. Kaluza, J. Schreiber, M. I. K. Santala, G. D. Tsakiris, K. Eidmann, J. Meyer-ter-Vehn, and K. J. Witte, *Phys. Rev. Lett.* **93**, 045003 (2004).
- [84] P. McKenna, K. W. D. Ledingham, J. M. Yang, L. Robson, T. McCanny, S. Shimizu, R. J. Clarke, D. Neely, K. Spohr, R. Chapman, R. P. Singhal, K. Krushelnick, M. S. Wei, and P. A. Norreys, *Phys. Rev. E* **70**, 036405 (2004).
- [85] T. Ceccotti, A. Lévy, H. Popescu, F. Réau, P. D’Oliveira, P. Monot, J. P. Geindre, E. Lefebvre, and P. Martin, *Phys. Rev. Lett.* **99**, 185002 (2007).
- [86] M. Nishiuchi, A. Fukumi, H. Daido, Z. Li, A. Sagisaka, K. Ogura, S. Orimo, M. Kado, Y. Hayashi, M. Mori, S. V. Bulanov, T. Esirkepov, K. Nemoto, Y. Oishi, T. Nayuki, T. Fujii, A. Noda, Y. Iwashita, T. Shirai, and S. Nakamura, *Phys. Lett. A* **357**, 339 (2006).

- [87] M. Nishiuchi, H. Daido, A. Yogo, S. Orimo, K. Ogura, J. Ma, A. Sagisaka, M. Mori, A. S. Pirozhkov, H. Kiriyama, S. V. Bulanov, T. Z. Esirkepov, I. W. Choi, C. M. Kim, T. M. Jeong, T. J. Yu, J. H. Sung, S. K. Lee, N. Hafz, K. H. Pae, Y.-C. Noh, D.-K. Ko, J. Lee, Y. Oishi, K. Nemoto, H. Nagatomo, K. Nagai, and H. Azuma, *Phys. Plasmas* **15**, 053104 (2008).
- [88] M. Borghesi, T. Toncian, J. Fuchs, C. A. Cecchetti, L. Romagnani, S. Kar, K. Quinn, B. Ramakrishna, P. A. Wilson, P. Antici, P. Audebert, E. Brambrink, A. Pipahl, R. Jung, M. Amin, O. Willi, R. J. Clarke, M. Notley, P. Mora, T. Grismayer, E. D'Humières, and Y. Sentoku, *Eur. Phys. J. Spec. Top.* **175**, 105 (2009).
- [89] M. Zepf, E. L. Clark, K. Krushelnick, F. N. Beg, C. Escoda, A. E. Dangor, M. I. K. Santala, M. Tatarakis, I. F. Watts, P. A. Norreys, R. J. Clarke, J. R. Davies, M. A. Sinclair, R. D. Edwards, T. J. Goldsack, I. Spencer, and K. W. D. Ledingham, *Phys. Plasmas* **8**, 2323 (2001).
- [90] Y. Murakami, Y. Kitagawa, Y. Sentoku, M. Mori, R. Kodama, K. Tanaka, K. Mima, and T. Yamanaka, *Phys. Plasmas* **8**, 4138 (2001).
- [91] A. Maksimchuk, K. Flippo, H. Krause, G. A. Mourou, K. Nemoto, D. Shultz, D. Umstadter, R. Vane, V. Y. Bychenkov, G. I. Dudnikova, V. F. Kovalev, K. Mima, V. N. Novikov, Y. Sentoku, and S. V. Tolokonnikov, *Plasma Phys. Rep.* **30**, 473 (2004).
- [92] M. Allen, P. K. Patel, A. Mackinnon, D. Price, S. Wilks, and E. Morse, *Phys. Rev. Lett.* **93**, 265004 (2004).
- [93] F. N. Beg, A. R. Bell, A. E. Dangor, C. N. Danson, A. P. Fews, M. E. Glinsky, B. A. Hammel, P. Lee, P. A. Norreys, and M. Tatarakis, *Phys. Plasmas* **4**, 447 (1997).
- [94] M. Tampo, S. Awano, P. R. Bolton, K. Kondo, K. Mima, Y. Mori, H. Nakamura, M. Nakatsutsumi, R. B. Stephens, K. A. Tanaka, T. Tanimoto, T. Yabuuchi, and R. Kodama, *Phys. Plasmas* **17**, 073110 (2010).
- [95] R. Prasad, S. Ter-Avetisyan, D. Doria, K. E. Quinn, L. Romagnani, P. S. Foster, C. M. Brenner, J. S. Green, P. Gallegos, M. J. V. Streeter, D. C. Carroll, O. Tresca, N. P. Dover, C. A. J. Palmer, J. Schreiber, D. Neely, Z. Najmudin, P. McKenna, M. Zepf, and M. Borghesi, *Nucl. Instrum. Methods A* **653**, 113 (2011).
- [96] A. G. Zhidkov, A. Sasaki, I. Fukumoto, T. Tajima, T. Auguste, P. D'Oliveira, S. Hulin, P. Monot, A. Y. Faenov, T. A. Pikuz, and I. Y. Skobelev, *Phys. Plasmas* **8**, 3718 (2001).
- [97] M. Murakami and M. M. Basko, *Phys. Plasmas* **13**, 012105 (2006).
- [98] G. I. Dudnikova, V. Y. Bychenkov, A. Maksimchuk, G. Mourou, J. Nees, S. G. Bochkarev, and V. A. Vshivkov, *Phys. Rev. E* **67**, 026416 (2003).
- [99] A. Flacco, F. Sylla, M. Veltcheva, M. Carrié, R. Nuter, E. Lefebvre, D. Batani, and V. Malka, *Phys. Rev. E* **81**, 036405 (2010).
- [100] J. Schreiber, F. Bell, F. Grüner, U. Schramm, M. Geissler, M. Schnürer, S. Ter-Avetisyan, B. M. Hegelich, J. Cobble, E. Brambrink, J. Fuchs, P. Audebert, and D. Habs, *Phys. Rev. Lett.* **97**, 045005 (2006).
- [101] O. Jäckel, Ph.D. thesis, Physikalisch-Astronomische Fakultät Friedrich-Schiller-Universität Jena, 2009.
- [102] K. Zeil, S. D. Kraft, S. Bock, M. Bussmann, T. E. Cowan, T. Kluge, J. Metzkes, T. Richter, R. Sauerbrey, and U. Schramm, *New J. Phys.* **12**, 045015 (2010).